ORIGINAL ARTICLE

Geochemical characteristics and behaviour of elements during weathering and pedogenesis over karst area in Yunnan–Guizhou Plateau, southwestern China

Howard Omar Beckford[1] · Huashuo Chu[2,3] · Changshun Song[2,4] · Cheng Chang[1] · Hongbing Ji[1,2]

Abstract

A study of two typical red soil profiles, Gumu (GM-limestone) and Sanjiacun (SJC-dolomite) was conducted at Yunnan–Guizhou Plateau, China. The study employed mineralogy, geochemical and elemental ratios to assess the mobilisation and distribution of elements during weathering and pedogenesis. The mineralogy results revealed similarity in distribution of secondary minerals in both profiles, with exception at the ferricrete layer. The results revealed inheritance relationship between red soils and their underlying bedrocks indicating that clay minerals were likely derived from in situ weathering products or metasomatic process rather than detrital process. During weathering and pedogenesis process, alkaline elements such as K and Rb behave similarly and were closely related. All lanthanide elements except for Ce shared similar transport trend with Y and Be; however, Be exhibited significant enrichment at ferricrete layer of the dolomite profile. Transitional elements such as Co and Mn behave similarly; while, the High Field Strength Elements (HFSE) were stable, except for Th and Sc which indicate depletion in upper soil layer of the dolomite profile. Our findings further revealed that both profiles have experienced intense chemical weathering with high Chemical Index of Alteration values (CIA: 83–93) and a constant Ba/Sr ratio > 2. Overall, both profiles experienced similar elemental behaviour with the accumulation of major elements, the leaching of alkaline earth elements and the fluctuation of trace elements including Rare earth elements (REEs). The elemental behaviour was primarily controlled by redox reaction, pH, water availability, ionic radii and the stability of secondary oxides/hydroxides. Our study further highlights the use of newly proposed geochemical proxy Fe/Na ratio, which revealed high correlation ($R^2 \approx 0.90$) with U, Ba, Zn, Cu, Mo, Ni, Sb and REEs of power functions. These findings indicate that Fe/Na ratio may be used to investigate the behaviour of trace elements including REEs in highly weathered soils.

Keywords Geochemical · Mineralogy · Weathering · Pedogenesis · Karst

Howard Omar Beckford and Chu Huashuo contributed equally to this work.

✉ Hongbing Ji
  ji.hongbing@hotmail.com

1 School of Energy and Environmental Engineering, University of Science and Technology Beijing, Xueyuan Road No. 30, Haidian District, Beijing 100083, People's Republic of China

2 State Key Laboratory of Environmental Geochemistry, Institute of Geochemistry, Chinese Academy of Sciences, Guiyang 550081, People's Republic of China

3 University of the Chinese Academy of Sciences, Beijing 100049, People's Republic of China

4 Guizhou Provincial Key Laboratory of Geographic State Monitoring of Watershed, Guizhou Education University, Guiyang 550018, People's Republic of China

Introduction

The red soils over carbonate rocks are widely distributed throughout the Mediterranean climatic region, and their origins in regards to the fundamental of parent material and pedogenesis remain a conflict (Lucke and Baumler 2012; Šušteršič et al. 2009). In the past, the term *terra rossa* was commonly referred to all red soils derived from limestone in the Mediterranean region (Bates and Jackson 1987). Presently, *terra rossa* is defined as reddish clayey to silty-clayey material occurring above limestone and dolomite in the form of a discontinuous layer, ranging from a few centimetres to several metres in thickness (Durn et al. 1999, 2007, 2013, 2014). Researchers from all across the world have put forward several theories to explain the origin of red soils, to include (1) detrital,

(2) metasomatic, (3) residual and modified residual, (4) allochthonous, (5) eolian, (6) iso-volumetric weathering, and (7) poly-original theories (Feng et al. 2009). Basically, these theories can be ascribed to two main viewpoints, differed by detrital and residual origin (Šušteršič et al. 2009). According to the detrital theory, red soils were formed due to the accumulation of alluvial mud, volcanic ash, or eolian dust on limestone (Muhs and Budahn 2009). While the metasomatic theory is based upon the phenomenon of authigenic clay replacement of limestone downward from the reaction front (Banerjee and Merino 2011; Dobrovolsky 1987; Li et al. 2000; Merino and Banerjee 2008). The residual theory proposed that *in situ* weathering provides a major portion of source material for the upper layers (Gong et al. 2010; Ji et al. 2004a, b; Moresi 1988; Walter et al. 1995; Wang et al. 1999; Wang and Feng 2004; Zhang et al. 2015). However, all of these theories have their own particular sets of limitations due to their geological and weather conditions (Lucke et al. 2012, 2014; Merino and Banerjee 2008). In addition, the later polygenic model of provenance also provides reasonable explanation for the evolution of red soil crust (Bautista et al. 2011).

Red soils are widely distributed in tropical and subtropical area of China, occupying a total area of 0.45 million km^2 (Zhao 1996). These soils include latosols, lateritic red soils, red earths, yellow soils, and red paddy soils derived from zonal soils. The soils from these profiles are mostly equivalent to oxisols, ultisols and some alfisols according to the soil taxonomic classification of USA. Yunnan–Guizhou (YG) Plateau in southwest China is comprised of highly developed red soils. The plateau was formed over the Cenozoic period and has a wide distribution of surface red soil crusts (Duan et al. 2001; Huang et al. 1998; Wang et al. 2012). Several studies on weathered carbonate crusts over the YG Plateau provided essential information for understanding karstic pedogenesis and provenance of red crust (Feng et al. 2012; Feng and Zhu 2009; Ji et al. 2004a, b). However, presently, the provenance of weathering carbonate crusts over southern China has been a long-standing debate (Boeglin and Probst 1998; Li and Zhu 2004; Zhu and Li 2002). Lu (1986) proposed that the clastic rocks over carbonate rock were due to remnants of weathering processes. Other studies such as Li et al. 1996; Li et al. 2000; Li et al. 2002; Zhu et al. 1996; Zhu and Li 2002 emphasised the significant effect of groundwater on the pedogenesis process, whereby elements are dissolved, metasomatised, and precipitated by meteoric fluid. Xi 1991 and Zhu 1993 also suggested that the red crust of China was derived from the weathering products of Quaternary sediments. While, Ji et al. 2004a, b proposed that the red soils over dolomite of YG plateau were the results of long-term accumulation by acid-insoluble residue during two-stage weathering process over the years.

The type and intensity of pedogenesis process may depend on soil environmental conditions and elemental ratios can be valuable indicators of past climatic conditions (Buggle et al. 2011) as well as weathering indices. A number of weathering indices are widely used for pedogenesis intensity (Buggle et al. 2011); these include the Index B of Kronberg and Nesbitt (1981), Chemical index of alteration (Nesbitt and Young 1982), Chemical Index of Weathering (Harnois 1988), the Plagioclase Index of Alteration (Fedo et al. 1995) and the Chemical Proxy of Alteration (Buggle et al. 2011). Sheldon and Tabor (2009) reviewed major element ratios commonly applied to individual pedogenesis process. The indices are based on the relationship between soluble or mobile elements and insoluble or immobile elements (Smykatz-Kloss 2003; Yang et al. 2004). For example, Iron (Fe) is a redox-dependent element which is usually excluded in the choice of weathering index (Buggle et al. 2011); however, Garrett and Lalor (2005) proposed that Fe/Na ratio can be used to determine soil maturity, based on the contrasting behaviour of Fe (enrichment) and Na (depletion) during pedogenesis. The study has found a U-shape relationship between several trace elements and Fe/Na ratio; therefore, in this paper, Fe/Na ratio was applied to both weathering profiles. In addition, the mobilisation and enrichment of elements in weathering profile can be determined by mass transport calculation (Anderson et al. 2002; Brimhall and Dietrich 1987), which reveal elements behaviour relative to immobile elements during weathering and pedogenesis. This study, therefore, examined the behaviour and distribution of major, trace and rare earth elements (REEs) with qualitative analysis of clay minerals, and explored the use of elemental ratios, in particular Fe/Na ratio in weathering and pedogenesis process of two red soil carbonate profiles at YG Plateau, southwestern China.

Materials and methods

Regional geology setting and sampling

The study area is located in the karst region of Yunnan–Guizhou Plateau, southwestern China which is approximately 11,100 km^2 (Duan and Tao, 2012). The Yunnan Province has a typical subtropical monsoon climatic with an average annual temperature range of 10–20 °C and an average annual rainfall of 1100 mm. The region has a distinct dry autumn–winter season and a wet spring–summer season. The monsoonal climate strongly influenced soil distribution, with red soils occurring to the west and yellow soils occurring to the east (Ji et al. 2004a, b). The Yunnan–Guizhou plateau has a wide deposit of developed red soil (Duan et al. 2001; Wang et al. 2012) and is part of the largest distribution of karst in the world (Yuan 1992). The spatial distribution

of soils is significantly discontinuous, with soil thickness ranging from a few cm to 365 cm.

Figure 1 illustrates the map of the study area location and lithology. The weathering profiles are the Sanjiacun (SJC) profile (23°15′16.44″N, 104°16′28.35″E) and the Gumu (GM) profile (24°42′27.96″N, 102°32′46.88″E) which are located in the upland region of karst terrain in Yunnan province, west of Yunnan–Guizhou Plateau (Fig. 1). The plateau comprised mainly of Proterozoic clastic sedimentary rocks and Palaeozoic to Upper–Middle Triassic marine carbonate rocks and post Triassic rocks that are mostly fluvial (Ji et al. 2004a, b). The profile drawing of SJC and GM is represented in Fig. 2. The soil profile of SJC is approximately 365 cm thick and consists mainly of limestone intercalated with dolomite. The Gumu soil profile comprised of limestone, slate intercalated with dolomite and a soil thickness of approximately 160 cm.

The exposed soil layer was removed and fresh soil samples were collected from the surface downward to the bedrock. The upper surface comprised of loose soil covered with sparse vegetation. Soil samples were collected at 20-cm and 10-cm intervals for SJC and GM soil profiles, respectively. Immediately below the top soil surface layer, there was distinct red soils layer with silty-clay and clay (SJC-20 to SJC-3 and GM-18 to GM-3). The sample layers SJC3 and GM3

were considered as the weathering front with strong plasticity and semi-weathered bedrocks, and SJC9 was the ferricrete layer (Fig. 2b). There was no ferricrete layer observed at GM soil profile (Fig. 2a). A noticeable strong weathered dolomite and limestone powder layers (SJC-2 and GM-2) which is about 2 cm thick covers the slightly weathered dolomite and limestone bedrocks (SJC-1 and GM-1) respectively (Fig. 2a, b). A total of thirty-eight (38) soil samples were collected from both profiles (20 in SJC and 18 in GM soil profiles).

Methods

The soil type was determined by comparing soil samples with the standard colour according to the Munsell Book of Color (X-Rite, Grand Rapids, MI, USA). Fresh soil samples were collected from the representative horizons of the soil, saprolite, slightly/strongly weathered bedrock and bedrock at a 10-cm interval (Fig. 2), and preserved in zip-lock bags (c. 0.5 kg). The soil samples were later then transported to the laboratory, air dried, grounded with an agate mortar and sieved through a 200-mesh size (74um) light sieve, and then stored in polyethylene bags for further analysis. The pH of soil samples was determined using 1-N KCl solution in a 1:2.5 ratio of soil/solution.
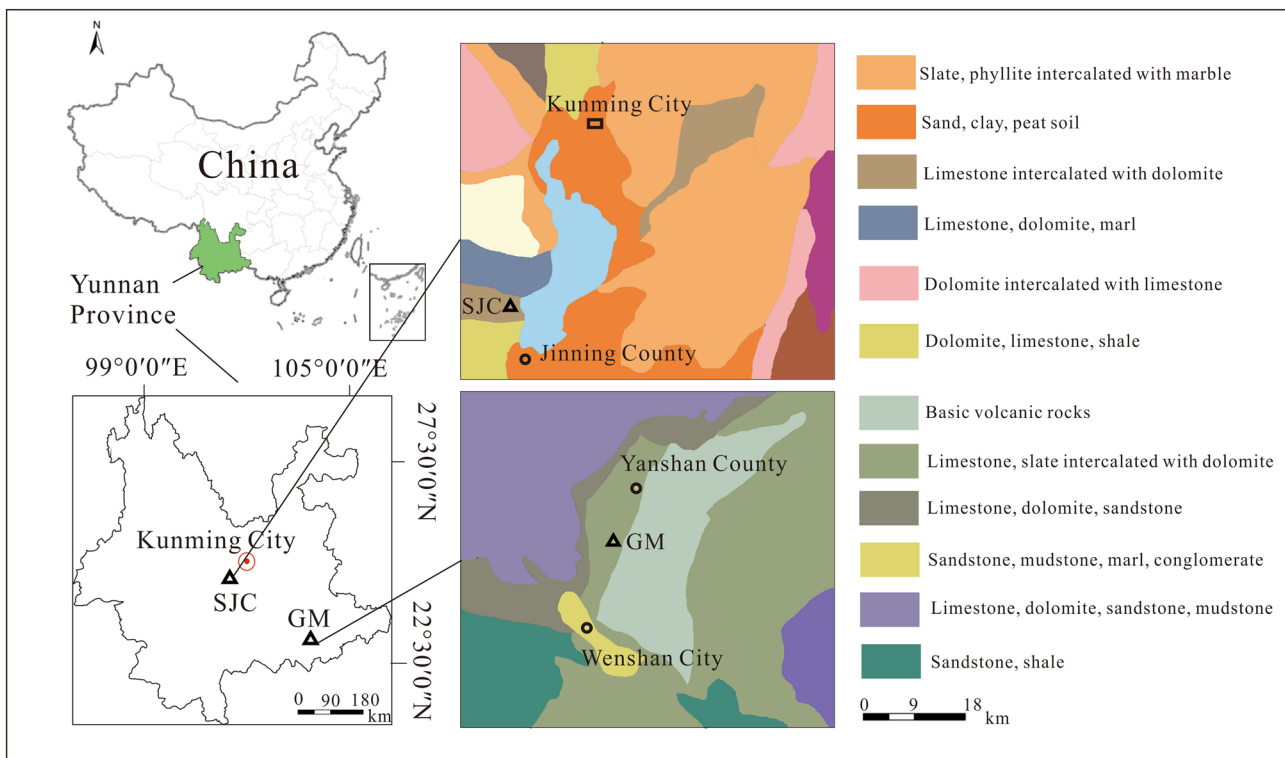

Fig. 1 Map showing location of study area, sample profiles location and lithology of sample profiles for Sanjiacun (SJC) and Gumu (GM) at Yunnan-Guizhou, Southwestern China.
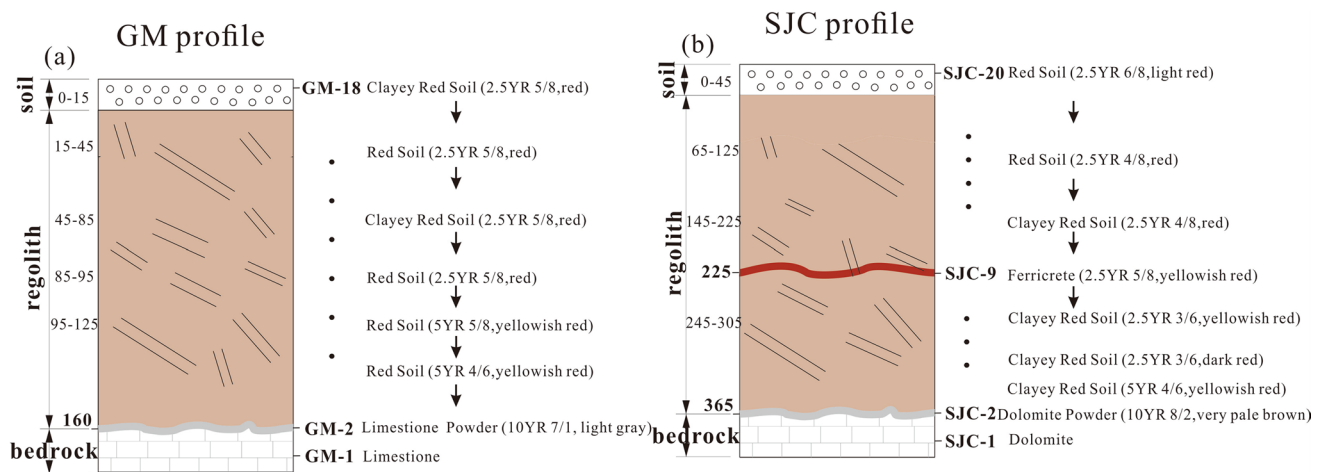
Fig. 2 Sample profiles representation of Sanjiacun (SJC) and Gumu (GM) at Yunnan-Guizhou Plateau, Southwestern China

The mineral composition analysis of the sieved bulk samples was carried out by X-ray diffraction at the State Key Laboratory of Ore Deposit Geochemistry, Institute of Geochemistry, Chinese Academy of Sciences. The analysis was carried out using the Dmax/2200 model (made by Japan), including the instrument standard CuKα target, 40 kV, 20 mA, scanning scope for 2–60°, scanning step length for 0.04°, and scanning speed for 10°/min. The major element oxides of the soil samples were determined by X-ray fluorescence spectrography (XRF) using Philips PW2404 X-ray fluorescence spectrometer, referring the GB/T14506.28-93 silicate rock chemical analytical procedure, at Analtical Laboratory of CNNC Beijing Research Institute of Uranium Geology.

Trace and rare earth element concentrations were measured by Inductively Coupled Plasma Mass Spectroscopy (ICP-MS) (Element I, Finnigan MAT Company) referring DZ/T0223-2001 ICP-MS procedure at a temperature of 20 °C and humidity of 30%, at the State Key Laboratory of Ore Deposit Geochemistry, Institute of Geochemistry, Chinese Academy of Sciences (SKLODG, IGCAS). First, 0.1 g of sample, 1.5-mL HF and 1-mL HNO_3 was added into teflon melting pot to dissolve the samples under closed condition. The sample pot was heated in a bake furnace at 140 °C; for 48 h after which it was placed on an electrothermal plate for cooling and then 1 mL of HNO_3 was added. This procedure was repeated; then 3-mL HNO_3 and 10-mL H_2O were added to dissolve the samples in a 100-mL plastic bottle for ICP-MS analysis. Using neutron activation method, the analyses were monitored with three standard samples (AGV-2, AMH-1, GBPG-1). The analytical uncertainties in measurements for major and trace elements are 1% and 10%, respectively.

Mass balance calculation

The mass balance calculation is commonly used to assess the mobilisation and distribution of elements during chemical weathering and pedogenesis processes (Babechuk et al. 2014, 2015; Brantley and Lebedeva 2011; Kurtz et al. 2000; Nesbitt 1979; Nesbitt et al. 1980). The mass fraction of element gain to or lost from soil during pedogenesis relative to the mass originally present in the parent material is calculated according to Eq. (1) (Anderson et al. 2002; Brimhall and Dietrich 1987).

$$\text{Mass balance of element } \tau_{ij} = \frac{C_{j,w}/C_{j,p}}{C_{i,w}/C_{i,p}}, \tag{1}$$

where C is the concentration of an element, w refers to the weathered material, the p refers to the parent material, and i refer to the least mobile element. Negative values of τ_{ij}, w indicate net loss of element from the weathered profile (w), and positive values define the extent of enrichment of element j in the soil profile.

In this study, the fresh parent rock is replaced by the weathering front soil layer for calculation, following several considerations. First, the large volume change from the bedrock to regolith in carbonate profiles may reduce or magnify geochemical changes if the calculation is based on bedrock (Ji et al. 2004b). Second, the SJC and GM bedrocks are slightly weathered (Tables 1, 3); furthermore, the analysis of the elements mobilisation, from weathering front to upper red soils, can give a better indication of pedogenesis (Zhang et al. 2015) (Tables 2, 4).

By referring to the "immobile plateau" method (Gong et al. 2011), Nb was determined as the immobile element in our subsequent discussion, although normalising Ta instead would produce similar results (Kurtz et al. 2000). This study

Table 1 The major and trace elements concentrations from GM profile

Samples	GM-1	GM-2	GM-3	GM-4	GM-5	GM-6	GM-7	GM-8	GM-9	GM-10	GM-11	GM-12	GM-13	GM-14	GM-15	GM-16	GM-17	GM-18
Petrography	Lime-stone	Lime stone powder	Red soil	Red soil	Red soil	Red soil	Red soil	Red soil	Red soil	Red soil	Red soil	Red soil	Red soil	Red soil	Red soil	Red soil	Red soil	Red soil
SiO_2	0.83	1.81	35.04	34.73	35.14	34.58	34.75	34.98	34.99	35.06	35.08	34.90	35.45	35.33	35.32	35.20	35.26	35.39
Al_2O_3	0.24	1.50	30.15	30.50	30.42	30.66	30.60	30.55	30.68	30.67	30.66	30.49	30.39	30.41	30.31	30.32	30.35	30.16
$Fe_2O_3^T$	0.10	0.67	14.75	14.71	14.64	14.75	14.74	14.68	14.52	14.49	14.57	14.67	14.46	14.58	14.64	14.61	14.61	14.61
MgO	0.49	0.60	0.92	0.87	0.90	0.86	0.86	0.89	0.87	0.88	0.89	0.89	0.87	0.88	0.85	0.86	0.87	0.85
CaO	53.97	51.81	0.29	0.23	0.24	0.15	0.16	0.14	0.13	0.13	0.12	0.13	0.12	0.13	0.13	0.13	0.14	0.14
Na_2O	0.19	0.04	0.08	0.07	0.07	0.08	0.08	0.07	0.07	0.07	0.08	0.08	0.08	0.08	0.07	0.08	0.08	0.08
K_2O	0.06	0.18	1.86	1.63	1.66	1.68	1.73	1.83	1.78	1.80	1.81	1.80	1.80	1.79	1.77	1.77	1.77	1.72
MnO	0.00	0.01	0.11	0.10	0.10	0.08	0.07	0.09	0.08	0.09	0.08	0.08	0.06	0.08	0.05	0.05	0.05	0.05
TiO_2	0.02	0.07	1.04	1.07	1.06	1.00	1.04	1.06	1.05	1.07	1.08	1.09	1.17	1.16	1.16	1.15	1.17	1.20
P_2O_5	0.01	0.01	0.10	0.11	0.11	0.11	0.10	0.10	0.10	0.10	0.10	0.10	0.10	0.10	0.10	0.10	0.10	0.11
LOI	43.54	42.74	15.27	15.50	15.33	15.64	15.43	15.28	15.36	15.27	15.23	15.19	15.14	15.15	15.09	15.30	15.03	15.26
CIA[b]	26	83	93	94	94	93	93	93	93	93	93	93	93	93	93	93	93	93
Li	1.07	7.62	148	130	131	129	127	130	126	126	128	126	140	136	132	127	132	129
Be	0.07	4.88	17.40	11.60	13.30	12.80	10.40	9.90	8.57	8.91	7.78	6.27	5.28	5.70	6.42	5.82	6.10	5.53
V	3.26	22.90	308	324	288	272	321	326	291	313	316	313	415	270	330	322	336	330
Co	4.50	6.51	104	62.20	59.50	48.30	47.70	52.70	49.60	51.60	52.80	48.90	42.50	49.70	34.50	34.40	35.10	35.60
Ni	18.7	28.1	246.9	231.6	231.6	234.2	233.3	238.4	227.4	235.0	235.0	229.1	236.2	223.0	214.8	214.8	218.1	211.5
Cu	1.32	5.00	94.61	94.61	95.44	93.78	92.95	93.78	93.78	95.44	93.78	92.12	98.71	95.53	91.55	93.14	93.93	94.73
Zn	5.4	22.5	440.0	443.0	445.0	452.0	449.0	452.0	423.0	451.0	431.0	441.0	471.4	382.1	384.8	379.4	392.8	382.1
Sr	156	187	34.60	36.60	35.20	34.80	34.20	34.00	34.50	36.10	35.40	35.80	39.10	42.50	71.90	46.50	40.90	41.20
Y	3.5	106.0	218.0	259.0	274.0	258.0	207.0	205.0	193.0	186.0	187.0	168.0	167.0	118.0	103.0	99.0	94.9	85.1
Sc	1.02	2.65	33.90	33.90	35.40	33.70	34.90	33.10	32.10	33.20	33.00	32.70	37.00	33.70	34.40	32.00	33.50	34.20
Zr	2.0	15.4	240.0	244.0	253.0	236.0	244.0	260.0	245.0	262.0	252.0	254.0	281.0	273.0	274.0	267.0	280.0	288.0
Nb	0.23	1.57	24.55	25.02	25.57	24.00	24.55	25.18	24.79	25.81	25.57	25.65	27.65	27.34	27.18	27.42	27.26	28.50
Ta	0.07	0.39	3.49	3.37	3.28	3.08	3.20	3.24	3.26	3.30	3.38	3.33	3.33	3.56	3.58	3.63	3.50	3.72
Th	0.23	3.67	30.60	29.50	29.00	28.70	28.90	29.30	28.90	29.80	29.30	29.70	29.87	29.60	29.56	29.34	28.69	29.25
U	0.46	1.88	11.90	11.20	11.00	10.70	11.50	12.90	13.10	13.10	13.50	12.90	11.10	11.70	11.90	11.34	11.19	11.25

GM Gumu profile

Major elements measured in (wt. %): trace (µg/g)

$CIA = [Al_2O_3/(Al_2O_3 + CaO^* + Na_2O + K_2O)] \times 100$

LOI loss on ignition

has summarised the transport coefficiencies of elements (Fig. 8), with a margin of error ± 0.2 for $\tau_{ij,w}$ considered (Braun et al. 2012; Wei et al. 2014).

Elemental ratios

To evaluate the intensity of chemical weathering and pedogenesis, different indices based on bedrock geochemical analyses have been proposed. In this paper, several types of proxies have been employed to characterise element source or provenance, element mass flux and weathering intensity of regolith. These proxies included (1) Major element concentration ratios, (2) Trace element concentration ratio, Chemical Index of Alteration (CIA) (Nesbitt and Young 1982), and (4) Mass balance calculation.

Results

Geochemical characteristics

Tables 1 and 3 listed the major and trace elements, while Tables 3 and 4 listed the rare earth elements concentrations and other parameters including Loss On Ignition (LOI) and CIA for GM and SJC soil profiles, respectively, in Yunnan–Guizhou Plateau, southwestern China. Major element oxides such as Al_2O_3, SiO_2, Fe_2O_3 and LOI of red soils layers accounted for 95% of the total soil mass, with the others accounting for the remaining percentage. The red soils are characterised by enrichment of SiO_2, $Fe_2O_3^T$, and Al_2O_3 in comparison to the bedrock and rock powder. More specifically, the soil and saprolite from the GM weathering profile comprised of relatively high Al_2O_3 (30.15–30.66%), SiO_2 (34.58–35.45%), Fe_2O_3 (14.46–14.75%) and TiO_2 (1–1.2%) which are several times higher than the bedrock and bedrock powder. Meanwhile, P_2O_5 and MnO content values ranged between 0.1–0.11% and 0.05–0.10%, respectively. Similarly, the SJC weathering profile contains high amount of Al_2O_3 (13.2–36.3%), SiO_2 (31.5–73.6%), Fe_2O_3 (5.9–26.2%) and TiO_2 (0.7–1.7%), with the minimum concentration of SiO_2 in the ferricrete layer, and the maximum values for MnO (0.05–0.11%) and P_2O_5 (0.1–0.11%) in the ferricrete layer. In comparison, the range of alkali elements in the soil and saprolite was CaO (0.12–0.29%), Na_2O (0.07–0.08%), K_2O (1.63–1.86%) and MgO (0.85–0.92%) for the GM weathering profile. The CaO and Na_2O contents are distinctly lower than the bedrock value, while K_2O and MgO are higher than the bedrock value. Conversely, a similar trend is observed in SJC weathering profile for CaO (0.1–0.3%) and MgO (0.4–1.5%) where the values are lower than bedrock; however, a different trend is observed for Na_2O content which remains constant at 0.1%, and MgO content values which were higher and lower than the bedrock, respectively.

The pH value along vertical distribution is important for understanding of mineral variation and the pedogenic process. The red soils in Yunnan–Guizhou Plateau were found to have neutral or even slightly alkaline pH values due to the strong influenced of limestone (Fig. 3a). The pH values displayed different variations between the carbonate weathering profiles (Tables 2, 4; Fig. 3a). The rock powder layer displayed greater fluctuation in pH values for both profiles with a sudden increase at SJC profile and decrease at GM profile. The SJC red soils showed a relatively stable pH ≈ 8, while the GM red soils showed a gradually decrease in pH values from bottom of the profile to top soils (pH = 6–9) (Fig. 3a).

Mineral composition and distribution characteristics

The XRD analysis has been widely used to show mineral composition and distribution during weathering and pedogenesis. Figure 4 showed the XRD patterns of GM profile (A: top) and SJC profile (B: bottom), illustrating the changes in mineral compositions from the bedrock through to the upper layers of the red soil profiles. The GM rock powder layer (GM2) was comprised of calcite, montmorillonite and illite, which is similar to those in the bedrock (GM0). From weathering front (GM3) to red soil layers, the minerals kaolinite and montmorillonite were detected with the similar pattern to those in rock powder; meanwhile, secondary minerals such as kaolinite, vermiculite gibbsite, hematite and anatase were detected. The mineral composition of SJC rock powder layer (SJC2) is similar to those of its bedrock (SJC1), i.e. dolomite, illite, montmorillonite and quartz. From weathering front (SJC3) to red soil layers, the minerals montmorillonite, illite and quartz were present and are similar to those in the rock powder (SJC2); while secondary minerals such as kaolinite, gibbsite, diasporite, and anatase were detected (Fig. 4).

Major and trace elements composition and distribution

The major and trace elements (Tables 1, 3) in the soils are normalised by average upper continental composition (UCC) and compared with geochemical data from GM and SJC profiles as shown in Fig. 5. In comparison to UCC, the GM profile was significantly enriched in Be and Y at the rock powder layer, and enriched with Li, Be, V, Co, Ni, Cu, Zn, Y, Sc, Nb, Ta, Th, U, Al, Ti in the red soil layers. While on the other hand, the SJC profile was significantly enriched in Y at rock powder, and enriched with Li, V, Co, Ni, Cu, Zn, Y, Sc, Zr, Nb, Hf, Ta, Th, U, Ti at the red soil layers. The rock powder of both profiles showed transitional status between bedrock and red soils. The red soils and rock powder displayed similar shape, except that there is depletion in

Table 2 The REE concentrations from GM profile

Samples	GM-1	GM-2	GM-3	GM-4	GM-5	GM-6	GM-7	GM-8	GM-9	GM-10	GM-11	GM-12	GM-13	GM-14	GM-15	GM-16	GM-17	GM-18
Petrography	Lime stone	Lime stone powder	Red soil	Red soil	Red soil	Red soil	Red soil	Red soil	Red soil	Red soil	Red soil	Red soil	Red soil	Red soil	Red soil	Red soil	Red soil	Red soil
La	2.41	81.90	177.00	166.00	161.00	159.00	150.0	154.0	142.0	136.0	141.0	132.0	127.0	96.50	96.00	101.0	99.40	94.80
Ce	2.9	13.9	171.0	149.0	155.0	141.0	163.0	161.0	147.0	166.0	160.0	172.0	237.0	179.0	160.0	173.0	183.0	201.0
Pr	0.37	32.90	82.40	72.00	72.80	71.60	60.60	61.30	59.80	56.70	57.80	53.60	40.90	34.30	30.30	31.00	29.10	25.80
Nd	1.6	158.0	365.0	321.0	319.0	316.0	265.0	263.0	254.0	246.0	250.0	226.0	163.0	135.0	118.0	121.0	113.0	100.0
Sm	0.22	55.40	92.40	84.90	84.20	83.50	67.70	68.10	66.80	62.30	64.10	59.60	37.60	33.10	27.60	27.00	25.40	20.80
Eu	0.07	13.82	19.03	18.20	18.33	17.76	14.43	14.31	14.17	13.58	13.39	12.15	8.78	7.55	6.33	5.76	5.19	4.26
Gd	0.33	65.98	82.06	80.55	83.71	79.75	66.59	64.53	63.41	59.87	59.26	53.83	36.54	33.91	27.86	24.55	22.64	18.89
Tb	0.06	11.10	14.00	14.00	14.20	14.00	11.40	11.10	11.10	10.40	10.50	9.50	5.72	5.00	4.24	4.13	3.69	3.09
Dy	0.31	49.10	69.10	72.60	74.30	69.80	58.40	58.30	57.80	54.00	54.20	49.70	34.80	29.60	25.10	24.70	22.10	19.10
Ho	0.07	8.72	14.80	15.70	15.90	15.10	12.80	12.20	12.30	11.60	11.70	10.80	7.57	6.56	5.57	5.26	4.81	4.08
Er	0.19	18.70	39.30	40.40	43.20	41.20	34.40	33.10	33.70	32.10	31.60	29.00	20.20	17.70	15.00	14.20	13.00	11.20
Tm	0.03	1.92	5.02	5.23	5.44	5.22	4.51	4.44	4.60	4.16	4.17	3.84	2.86	2.53	2.23	2.09	2.05	1.78
Yb	0.21	9.54	27.40	28.50	29.30	29.30	25.00	24.80	25.60	24.30	23.60	22.40	15.80	14.30	12.90	12.30	11.80	10.60
Lu	0.03	1.33	4.34	4.42	4.49	4.47	3.84	3.51	3.77	3.65	3.49	3.37	2.45	2.25	1.94	1.98	1.86	1.62
$\sum$REE	8.71	522.3	1162.9	1072.5	1080.9	1047.7	937.7	933.7	896.1	880.7	884.8	837.8	740.2	597.3	533.1	547.9	537.1	517
$\sum$LREE	7.49	355.9	906.83	811.10	810.33	788.86	720.7	721.7	683.8	680.6	686.3	655.4	614.3	485.5	438.2	458.8	455.1	446.7
$\sum$HREE	1.22	166.4	256.02	261.40	270.54	258.84	216.9	211.9	212.3	200.1	198.5	182.4	125.9	111.9	94.84	89.21	81.96	70.36
$\sum$LREE%	85.9	68.14	77.98	75.63	74.97	75.29	76.86	77.30	76.31	77.28	77.56	78.22	82.99	81.27	82.21	83.72	84.74	86.39
$\sum$HREE%	14.1	31.86	22.02	24.37	25.03	24.71	23.14	22.70	23.69	22.72	22.44	21.78	17.01	18.73	17.79	16.28	15.26	13.61
$\sum$LREE/$\sum$HREE	6.12	2.14	3.54	3.10	3.00	3.05	3.32	3.40	3.22	3.40	3.46	3.59	4.88	4.34	4.62	5.14	5.55	6.35
$(La/Yb)_N$	5.37	3.96	2.98	2.69	2.54	2.50	2.77	2.87	2.56	2.58	2.76	2.72	3.71	3.11	3.43	3.79	3.89	4.13
$(La/Sm)_N$	6.35	0.87	1.13	1.15	1.13	1.12	1.31	1.33	1.25	1.29	1.30	1.31	1.99	1.72	2.05	2.21	2.31	2.69
$(Gd/Yb)_N$	0.85	3.66	1.59	1.50	1.51	1.44	1.41	1.38	1.31	1.30	1.33	1.27	1.22	1.26	1.14	1.06	1.02	0.94
Ce/Ce*	0.59	0.05	0.28	0.27	0.28	0.26	0.33	0.32	0.31	0.37	0.35	0.40	0.64	0.61	0.58	0.60	0.66	0.79
Eu/Eu*	0.09	0.08	0.07	0.08	0.07	0.07	0.07	0.07	0.07	0.08	0.07	0.07	0.08	0.08	0.08	0.08	0.07	0.07
pH-KCl	8.85	8.29	8.99	9.00	8.84	8.59	8.38	8.35	8.22	8.11	8.07	7.88	7.62	7.47	7.31	7.22	7.08	6.54

All concentrations are normalised to the bulk sample and given in µg/g

The Ce anomaly $(Ce/Ce^* = Ce_N/[(La_N + Pr_N)/2])$ and Eu anomaly $(Eu/Eu^* = Eu_N/[(Sm_N + Gd_N)/2])$ were calculated

Listed also the $(La/Yb)_N = ((La/La_N)/(Yb/Yb_N))$, $(La/Sm)_N = ((La/La_N)/(Sm/Sm_N))$ and $(Gd/Yb)_N = ((Gd/Gd_N)/(Yb/Yb_N))$ ratios indicating the degree of REE

Table 3 The major and trace elements concentrations from SJC profile

Samples	SJC-1	SJC-2	SJC-3	SJC-4	SJC-5	SJC-6	SJC-7	SJC-8	SJC-9	SJC-10	SJC-11	SJC-12	SJC-13	SJC-14	SJC-15	SJC-16	SJC-17	SJC-18	SJC-19	SJC-20
Petrography	Dolomite	Dolomite powder	Red soil	Red soil	Red soil	Red soil	Red soil	Red soil	Ferricrete	Red soil	Red soil	Red soil	Red soil	Red soil	Red soil	Red soil	Red soil	Red soil	Red soil	Red soil
SiO_2	0.5	5.0	61.2	73.6	45.8	51.0	45.1	37.8	31.5	38.3	40.1	38.0	36.4	58.1	66.2	70.9	63.4	64.1	61.2	53.4
Al_2O_3	0.2	2.9	18.1	13.2	27.4	23.0	25.6	29.0	23.2	27.6	27.3	28.4	36.3	21.3	16.7	14.1	18.4	17.4	18.3	23.7
$Fe_2O_3^T$	0.3	2.0	9.2	5.6	10.8	11.0	12.4	13.9	26.2	14.3	14.1	15.0	9.9	8.3	6.5	5.9	7.1	7.2	8.4	9.8
MgO	20.8	18.5	0.6	0.4	0.9	0.9	1.1	1.4	1.3	1.5	1.3	1.1	0.7	0.5	0.5	0.4	0.4	0.4	0.5	0.5
CaO	30.6	27.5	0.3	0.1	0.1	0.1	0.1	0.2	0.2	0.3	0.1	0.1	0.2	0.1	0.1	0.1	0.1	0.1	0.2	0.2
Na_2O	0.0	0.0	0.1	0.1	0.1	0.1	0.1	0.1	0.1	0.1	0.1	0.1	0.1	0.1	0.1	0.1	0.1	0.1	0.1	0.1
K_2O	0.0	0.7	1.5	1.5	3.1	3.0	3.5	4.3	3.8	4.5	4.1	3.4	2.5	1.7	1.5	1.5	1.4	1.4	1.4	1.4
MnO	0.0	0.1	0.1	0.1	0.0	0.0	0.0	0.0	0.2	0.1	0.0	0.0	0.0	0.0	0.0	0.0	0.0	0.1	0.0	0.0
TiO_2	0.0	0.1	1.1	0.7	1.3	0.9	1.0	1.0	0.9	1.0	1.0	1.0	1.7	1.3	1.1	1.1	1.3	1.3	1.2	1.4
P_2O_5	0.0	0.0	0.1	0.1	0.1	0.1	0.1	0.1	0.2	0.1	0.1	0.1	0.1	0.1	0.1	0.1	0.1	0.1	0.1	0.2
LOI	47.0	42.6	7.7	4.7	10.3	9.5	10.6	12.1	12.1	11.8	11.3	12.4	11.9	8.2	7.1	5.8	7.5	7.5	8.4	9.3
CIA[b]	61.0	77.1	91.1	87.7	88.2	86.5	85.8	85.2	83.6	83.2	85.0	87.5	92.5	90.5	89.8	88.2	90.9	90.5	90.6	92.6
Li	1.1	13.1	151.0	196.9	227.0	211.0	214.0	225.0	141.0	197.0	210.0	254.0	528.0	194.0	146.0	141.0	192.0	171.0	138.0	120.0
Be	0.2	1.5	2.0	2.7	3.6	4.4	5.2	5.7	19.9	11.5	5.3	4.1	4.2	3.0	3.7	2.5	2.4	1.8	3.3	3.0
V	4.5	48.7	176.0	215.0	203.0	216.0	225.0	255.0	308.0	259.0	230.0	250.0	218.0	183.0	149.0	131.0	148.0	144.0	154.0	183.0
Co	4.9	17.6	78.5	62.7	40.1	28.9	30.0	27.9	123.0	136.0	20.9	21.1	14.8	20.2	27.6	29.5	20.4	36.4	26.0	21.0
Ni	8.2	16.0	57.7	39.0	84.8	102.7	106.9	118.8	147.6	131.5	108.6	117.9	66.5	55.2	47.1	35.0	42.8	46.0	52.5	50.3
Cu	2.1	6.2	32.0	30.1	36.9	41.0	49.0	63.7	78.5	51.9	52.5	54.2	33.9	34.7	29.4	24.6	27.7	31.7	32.3	31.6
Zn	10.3	41.7	221.0	213.0	215.0	251.0	281.0	342.0	390.0	355.0	291.0	291.0	169.0	149.0	146.0	126.0	122.0	132.0	186.0	187.0
Sr	102.0	112.0	33.1	36.9	38.5	32.7	37.2	42.4	52.6	41.6	43.4	38.0	33.2	31.5	31.3	26.2	25.6	31.6	34.9	38.5
Y	0.8	39.2	31.5	32.5	35.0	43.6	43.8	53.0	198.0	85.2	46.7	40.1	39.2	38.9	34.3	36.3	34.2	39.6	44.7	45.4
Sc	0.5	7.2	25.4	25.8	23.7	27.7	26.0	29.6	31.3	28.7	27.0	25.6	15.8	17.1	15.4	13.3	15.0	14.4	16.8	17.8
Zr	9.3	69.7	268.0	260.0	276.0	278.0	265.0	221.0	315.0	222.0	247.0	249.0	320.0	308.0	365.0	307.0	369.0	398.0	374.0	427.0
Nb	0.2	5.4	20.1	23.0	26.6	20.6	22.4	23.2	21.7	22.9	23.8	23.1	35.2	27.2	22.4	19.9	23.1	23.8	23.4	28.9
Ta	0.2	0.7	2.7	2.8	3.7	2.8	3.1	3.3	3.4	3.2	3.6	3.3	5.1	3.4	2.9	2.7	3.0	3.2	3.1	3.7
Th	0.4	6.2	25.8	30.2	32.2	28.3	30.7	34.1	30.8	32.6	33.8	30.8	37.6	22.7	19.4	17.0	19.7	20.0	20.7	26.6
U	0.6	2.3	5.5	3.2	5.5	5.3	5.7	6.5	7.4	6.6	6.9	6.8	6.7	5.1	4.8	4.4	4.8	4.8	5.1	6.5

SJC Sanjiacun profile

Major elements measured in (wt. %): trace (µg/g)

CIA = [Al_2O_3/(Al_2O_3 + CaO* + Na_2O + K_2O)] × 100

LOI loss on ignition

Table 4 The REE concentrations from SJC profile

Samples	SJC-1	SJC-2	SJC-3	SJC-4	SJC-5	SJC-6	SJC-7	SJC-8	SJC-9	SJC-10	SJC-11	SJC-12	SJC-13	SJC-14	SJC-15	SJC-16	SJC-17	SJC-18	SJC-19	SJC-20
Petrography	Dol	Dol powder	Red soil	Red soil	Red soil	Red soil	Red soil	Red soil	Ferricrete	Red soil	Red soil	Red soil	Red soil	Red soil	Red soil	Red soil	Red soil	Red soil	Red soil	Red soil
La	0.8	31.4	51.4	28.2	51.8	55.6	60.8	71.6	139.0	116.0	63.3	59.0	47.9	45.4	44.4	42.2	38.8	44.4	51.2	55.7
Ce	1.7	26.2	107.0	90.6	158.0	139.0	170.0	190.0	219.0	377.0	109.0	98.1	95.1	88.9	99.1	87.3	88.7	105.0	112.0	102.0
Pr	0.1	7.3	10.4	5.9	11.7	13.0	15.0	17.7	50.3	32.5	15.0	13.2	10.9	10.1	9.6	9.0	8.6	10.4	12.1	12.1
Nd	0.6	31.7	36.3	20.5	41.2	48.5	55.8	66.4	230.0	129.0	53.7	47.0	38.8	35.1	33.4	31.2	31.3	36.5	44.2	42.3
Sm	0.1	5.4	6.2	3.9	7.3	9.0	10.8	13.6	74.2	26.6	10.2	8.7	7.0	6.5	6.3	6.2	5.9	6.9	8.7	8.1
Eu	0.0	1.2	1.3	0.8	1.4	1.8	2.1	2.9	19.0	5.5	2.2	1.7	1.5	1.2	1.2	1.3	1.1	1.4	1.7	1.6
Gd	0.2	6.1	5.2	3.6	6.8	8.2	9.3	12.7	91.6	26.0	9.7	7.6	6.3	5.5	5.4	5.3	5.9	6.6	8.3	7.6
Tb	0.0	0.9	0.9	0.7	1.1	1.4	1.5	2.3	16.3	3.8	1.6	1.4	1.2	1.1	1.0	1.0	1.0	1.1	1.4	1.3
Dy	0.1	4.3	5.3	3.9	5.9	7.2	8.2	11.9	85.5	18.5	9.0	7.1	7.0	6.0	5.4	5.6	5.2	6.5	7.7	7.6
Ho	0.0	1.0	1.2	0.9	1.4	1.6	1.8	2.5	17.7	3.8	2.0	1.6	1.5	1.4	1.2	1.2	1.2	1.4	1.7	1.7
Er	0.1	2.3	3.5	2.4	4.1	4.3	5.2	6.9	48.0	10.4	5.6	4.7	4.5	4.0	3.6	3.7	3.5	3.9	4.6	4.6
Tm	0.0	0.3	0.5	0.4	0.7	0.7	0.8	1.1	6.7	1.5	0.8	0.7	0.8	0.6	0.5	0.6	0.6	0.7	0.7	0.7
Yb	0.1	1.5	3.4	2.7	4.3	4.3	5.3	6.5	35.1	8.8	5.2	4.6	4.8	4.1	3.6	3.6	3.6	4.2	4.6	4.7
Lu	0.0	0.2	0.5	0.4	0.7	0.7	0.8	0.9	5.4	1.3	0.8	0.7	0.8	0.7	0.6	0.5	0.5	0.6	0.7	0.7
$\sum$REE	3.8	119.7	233.0	164.9	296.4	295.1	347.5	406.9	1037	760.7	288.1	255.9	228.0	210.6	215.4	198.6	195.9	229.7	259.6	250.7
$\sum$LREE	3.3	103.2	212.5	150.0	271.4	266.8	314.5	362.2	731.5	686.6	253.4	227.7	201.2	187.2	194.0	177.1	174.5	204.6	229.9	221.8
$\sum$HREE	0.5	16.5	20.4	14.9	25.0	28.3	33.0	44.7	306.2	74.1	34.7	28.2	26.8	23.4	21.4	21.4	21.4	25.1	29.7	28.9
$\sum$LREE%	86.6	86.2	91.2	91.0	91.6	90.4	90.5	89.0	70.5	90.3	88.0	89.0	88.2	88.9	90.1	89.2	89.1	89.1	88.6	88.5
$\sum$HREE%	13.4	13.8	8.8	9.0	8.4	9.6	9.5	11.0	29.5	9.7	12.0	11.0	11.8	11.1	9.9	10.8	10.9	10.9	11.4	11.5
$\sum$LREE/$\sum$HREE	6.5	6.2	10.4	10.1	10.9	9.4	9.5	8.1	2.4	9.3	7.3	8.1	7.5	8.0	9.1	8.3	8.2	8.2	7.7	7.7
$(La/Yb)_N$	7.1	12.3	8.9	6.3	7.1	7.7	6.8	6.5	2.4	7.8	7.2	7.7	5.9	6.5	7.4	7.0	6.5	6.2	6.7	7.0
$(La/Sm)_N$	3.9	3.6	5.2	4.5	4.4	3.9	3.5	3.3	1.2	2.7	3.9	4.2	4.3	4.4	4.4	4.3	4.1	4.0	3.7	4.3
$(Gd/Yb)_N$	1.5	2.5	0.9	0.8	1.0	1.2	1.1	1.2	1.6	1.8	1.1	1.0	0.8	0.8	0.9	0.9	1.0	1.0	1.1	1.0
Ce/Ce*	1.0	0.4	1.0	1.5	1.3	1.1	1.2	1.1	0.5	1.3	0.7	0.7	0.9	0.9	1.0	0.9	1.0	1.0	0.9	0.8
Eu/Eu*	0.7	0.7	0.8	0.8	0.7	0.7	0.7	0.7	0.8	0.7	0.8	0.7	0.8	0.7	0.7	0.7	0.7	0.7	0.7	0.7
pH-KCl	8.8	9.1	7.6	7.6	7.7	7.7	7.6	7.6	7.5	7.7	7.9	7.9	7.8	8.2	8.3	8.4	8.6	8.4	8.2	8.1

All concentrations are normalised to the bulk sample and given in µg/g. Dol = Dolomite

The Ce anomaly $(Ce/Ce^* = Ce_N/[(La_N + Pr_N)/2])$ and Eu anomaly $(Eu/Eu^* = Eu_N/[(Sm_N + Gd_N)/2])$ were calculated

Listed also the $(La/Yb)_N = ((La/La_N)/(Yb/Yb_N))$, $(La/Sm)_N = ((La/La_N)/(Sm/Sm_N))$ and $(Gd/Yb)_N = ((Gd/Gd_N)/(Yb/Yb_N))$ ratios indicating the degree of REE

Fig. 3 Depth distribution profile characteristics of pH, Fe^{2+}/Fe^{3+} (mol.%), $Fe_2O_3^T$/Na_2O (wt.%), Ti/Al (mol.%), U/Th (ppm, UCC normalised), Ba/Sr (ppm, UCC normalised) for soil profiles of Sanjiacun (SJC) and Gumu (GM) profile in Yunnan–Guizhou Plateau, southwestern China. Fe^{2+}/Fe^{3+} = (FeO, mol.)/($Fe_2O_3^T$–FeO, mol), calculated according to Table 1
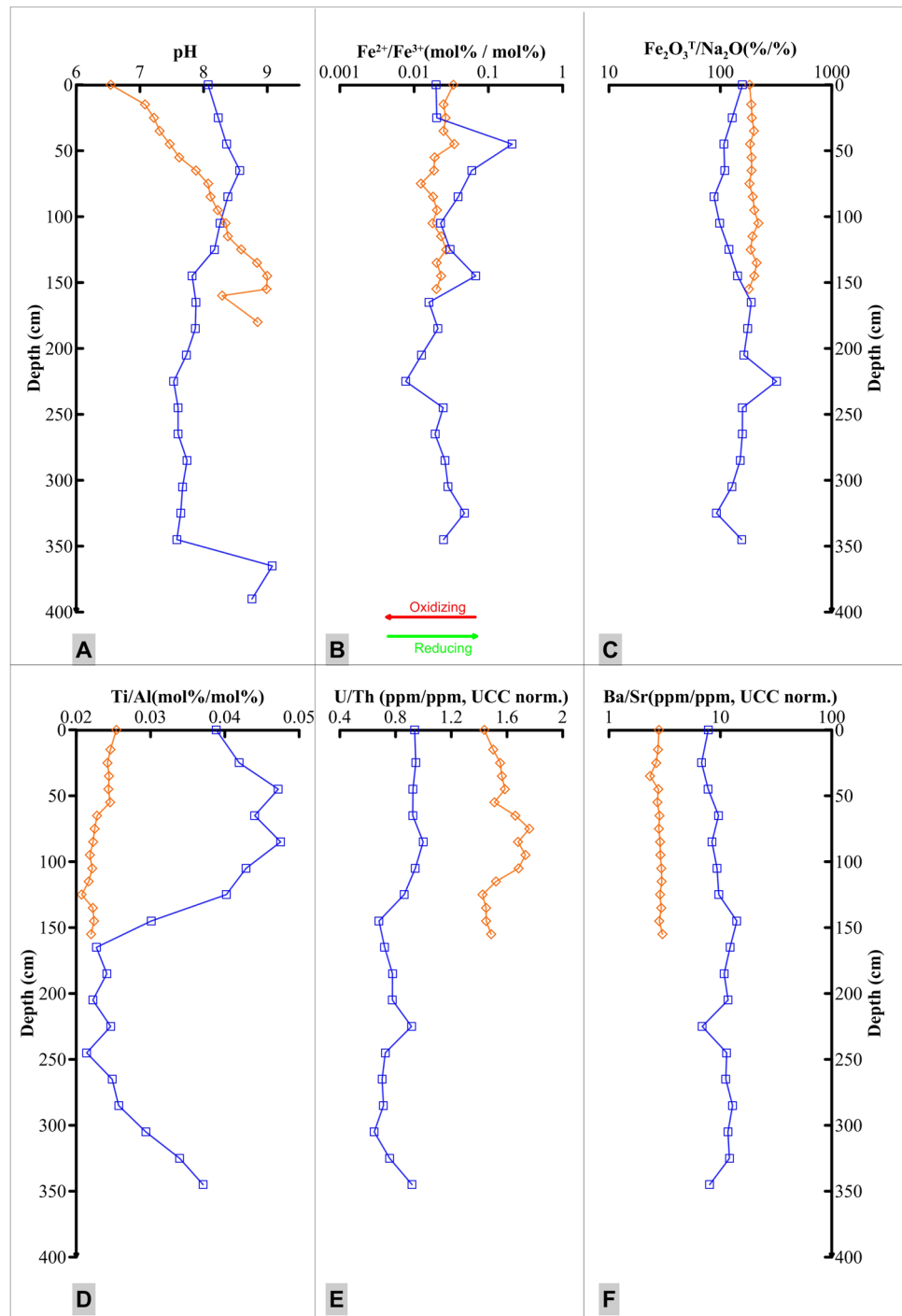
Sr in both profiles which may be due to the sensitive nature of Sr during weathering process.

Rare earth elements (REEs) composition and distribution

Tables 2, 4 and Fig. 6b, d illustrate normalised REE values for GM and SJC profiles, respectively. The REE pattern of GM profile indicates light-REE enrichment (Fig. 6a), and REE clustered with similar trends with slight negative Eu and Ce abnormalities at red soil layers, except for the strong negative Ce abnormality at rock powder layer. The red soils shared similar pattern with bedrock and rock powder. The SJC profile REE distribution exhibited similar light-REE enrichment (Fig. 6c), and REE clustered with similar trends with negative Eu abnormality. The rock powder layer

Fig. 4 X-ray diffraction (XRD) patterns for soil profiles of (top) Gumu (GM) and (bottom) Sanjiacun (SJC) profile in Yunnan-Guizhou Plateau, Southwestern China
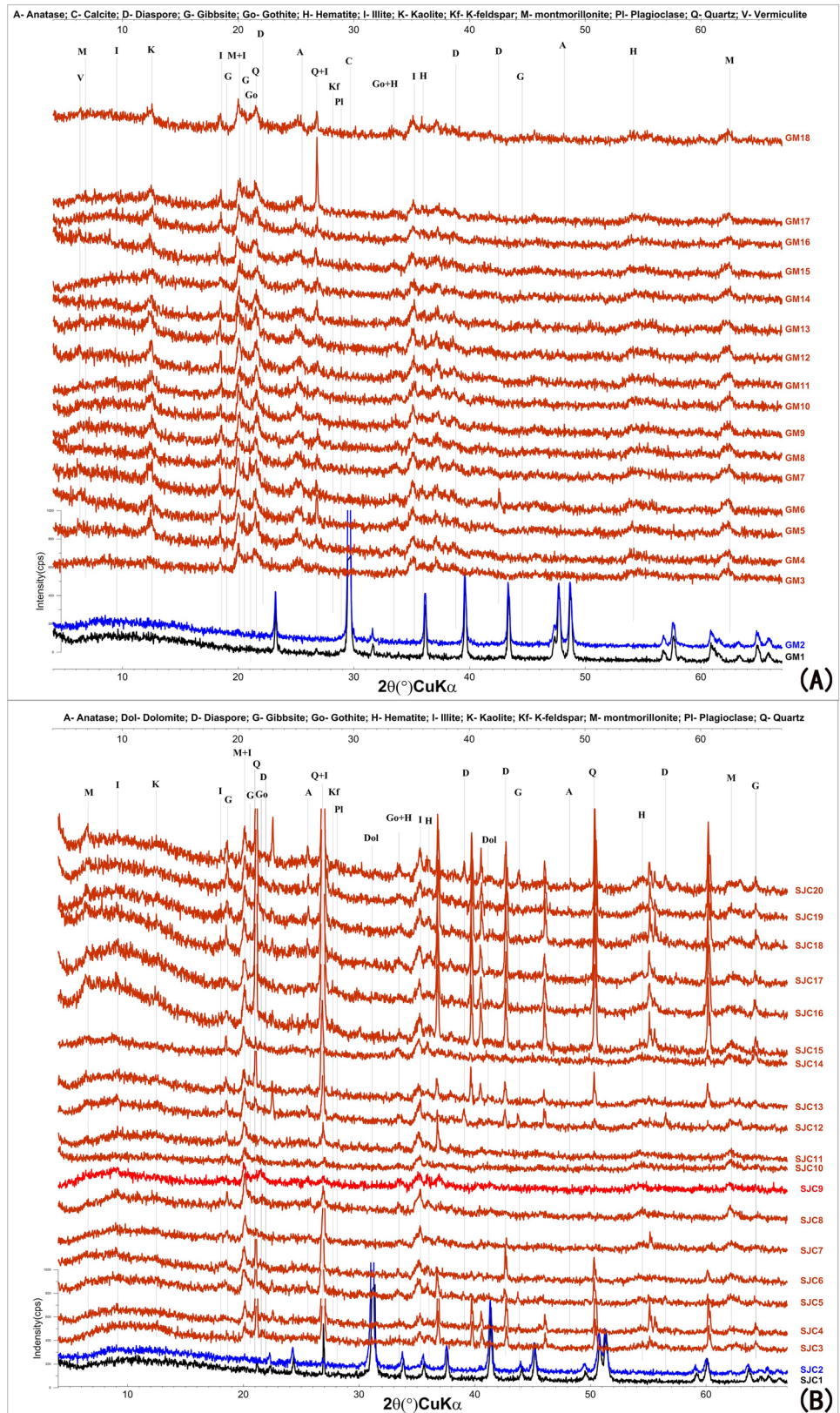
showed significantly negative Ce abnormality and slight negative Eu abnormality, which is similar to the bedrock. However, there were positive Ce abnomalities at the red soil layers.

Fig. 5 UCC-normalised spider diagrams for soil profiles of (top) Gumu (GM) and (bottom) Sanjiacum (SJC) in Yunnan–Guizhou Plateau, southwestern China. The UCC values are from Taylor and McLennan (1985). The element order follows Ji et al. (2004a)
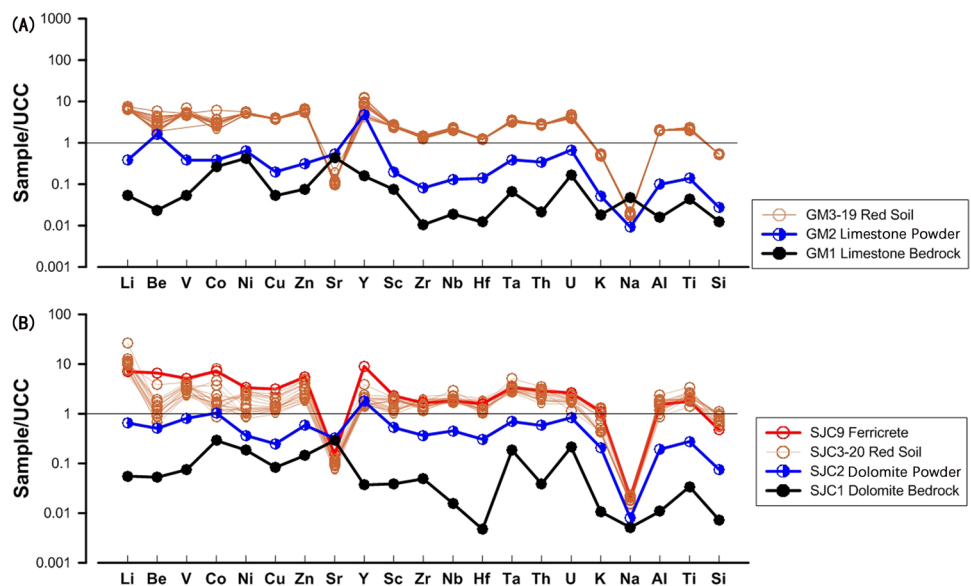
It is noticable that each profile have one layer with high total REEs concentration (Table 1, and Fig. 6a, c). The maximum total REEs of GM profile occurred at weathering front layer (GM3), and not at the powdered bedrock layer. This may be resulted from the unique conditions under which red soils developed in subtropical monsoonal climate with high oxidating pedogenesis at YG Plateau. However, the maximum total REE of SJC profile occurred at the ferricrete layer (SJC9), which may be due to the significant enrichment of REEs at the ferromanganese concretion. Both Niobium (Nb) and Tantalum (Ta) have + 5 valences, making them insoluble which accounts for their conservative behaviour. Nb was the least mobile element during peodogenesis in Mississipian paleosols when compared to other refactory elements (Babechuk et al. 2014; Kahmann et al. 2008; Widdowson and Cox 1996). Therefore, Nb may be used as an index element to evaluate gain or lost of other elements during pedogenesis. Nb and Ta were the least mobile elements in these studied soil profiles as Nb/Ta remain constant along the GM and SJC profiles (Fig. 7).

Mass balance calculation

The results obtained from the mass balance calculation revealed the following:

i. Major elements with Rb: transport coefficiency (τ) of Na, Mg, K, Si, P and Rb remain almost within the ± 0.2 margin of error in GM profile, indicating relative stability during weathering in comparison to the weathering front layer. However, Ca is depleted indicated by the transport coefficient τ of approximately -0.5 (Fig. 8a). Similarly, within the SJC profile, Ca

is also depleted except for the point at the ferricrete layer (SJC9) with the transport coefficient τ of Mg, K and Rb displayed enrichment around the ferricrete layer (SJC9). The element P is stable except for the enrichment at the ferricrete layer (SJC9). Si is lost while Mg, K and Rb are enriched below the SJC13 layer; however, above the SJC13 layer, elements K, Si, P, Na and Rb remain relatively stable, while Na is partly lost (Fig. 8e).

ii. REEs, Y with Be: except for Ce, all the lanthanide elements with Y and Be showed a gradual depletion at GM profile, while relatively stable except for enrichment at ferricrete layer in SJC profile. In GM profile, Ce remains stable except for a slight enrichment at GM13 layer (Fig. 8b). In SJC profile, Ce reached the highest enrichment point above ferricrete SJC9 layer. The transport coefficient τ of Co and Mn had similar depletion trend at both profiles, with an enrichment peak relative to adjacent layers at ferricrete layer SJC9 (Fig. 8b, f).

iii. Transitional elements Zn, Cu, Co, Ni, Cr with Fe, Mn, Al: the transport coefficient τ of Fe, Al, Zn, Cu, and Cr were similar at each profile. They were relatively stable in GM profile while in SJC profile, the transport coefficient τ of Fe, Al, Zn, Cu displayed enrichment around the ferricrete layer, except for the slight loss of Al relative to Fe which occurred at ferricrete layer SJC9. Each profile displayed similar transport coefficient τ of Co and Mn. In the GM profile, there was a gradual lost; while in the SJC profile, there was depleteion during pedogenesis, except for enrichment at the ferricrete layer. Co was enriched at SJC10 above the ferricrete layer, whereas Mn was depleted (Fig. 8c, g).
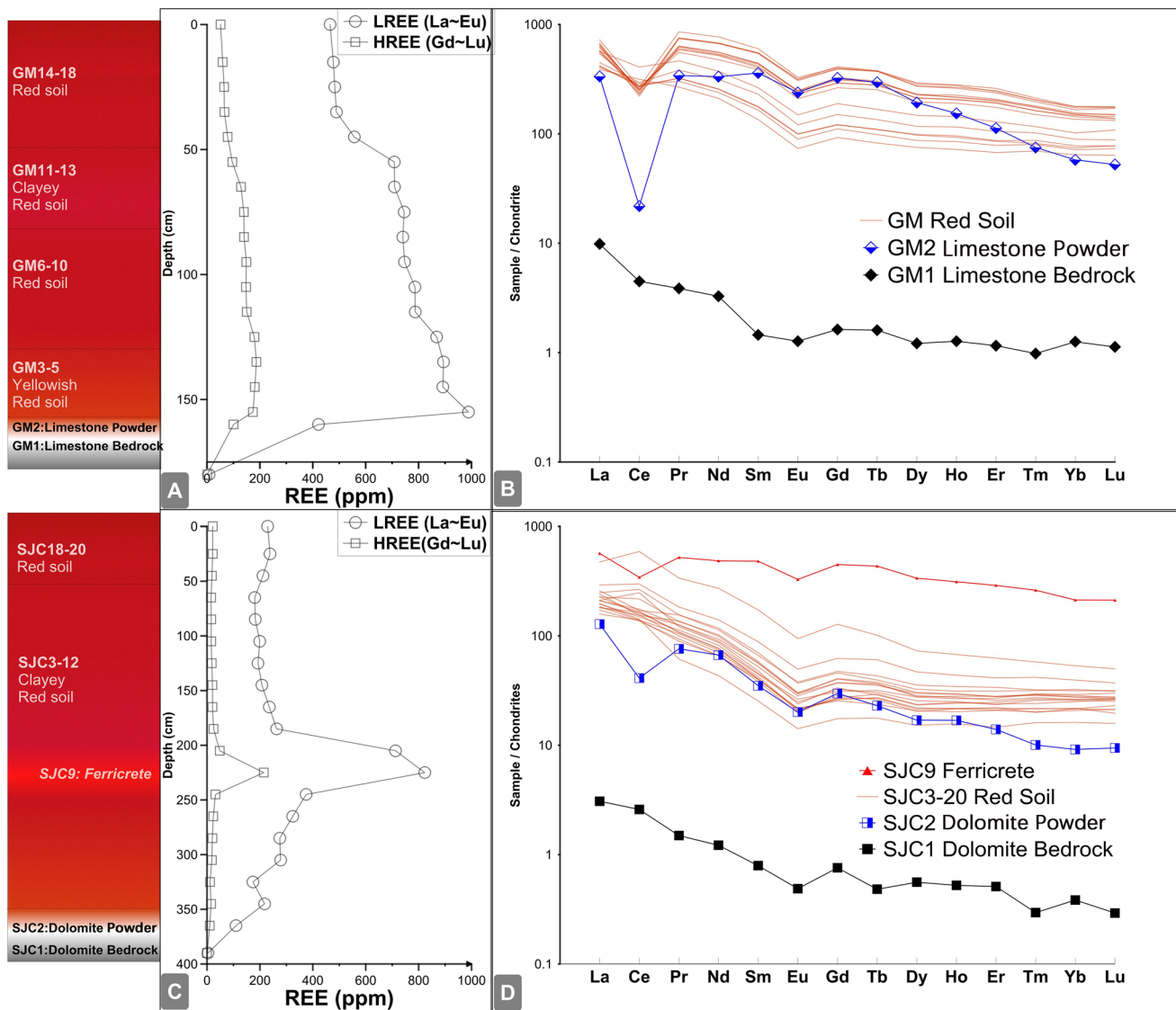
Fig. 6 LREE, HREE variation (left) and Chondrite-normalized REE patterns (right) of samples from the Gumu (GM) and Sanjiacum (SJC) profiles in Yunnan-Guizhou Plateau, Southwestern China. Normalized to the concentration in (Palme and Jones 2005)

iv. High Field Strength Elements (HFSE) such as Zr, Hf, Th, Ti, Ta, and Sc were examined in GM and SJC profiles. Our result revealed that Zr, Hf, Th, Ti, Ta, Sc were stable in GM profile, and were relatively stable in SJC profile below the SJC13 layer; however, depleted in Sc and Th, while slightly enriched in Hf above the SJC13 layer (Fig. 8d, h), respectively (Fig. 9).

Elemental ratios

The $Fe_2O_3{}^T/Al_2O_3$ ratio is an index used to evaluate in situ weathering. The relationship between Al_2O_3 and $Fe_2O_3{}^T$ is shown in Fig. 10. The samples in SJC (except for SJC13

and ferricrete layer SJC9) and GM profile showed a positive linear correlation, which indicates no obvious addition of external materials during the development of profile from the bedrock to upper rock powder for the red soils. The point SJC13 showed a slight increase of Fe^{2+}/Fe^{3+} (more reducing condition) and pH (as shown in Fig. 3a, b), respectively, which could increase the solubility of Fe in the reducing and acid solution. Similarly, TiO_2/Al_2O_3 ratio may be used to determine origin or source of material. The GM red soils layer displayed constant TiO_2/Al_2O_3 along the vertical profile as shown in Fig. 3d. However, samples from SJC9 to SJC20 exhibited higher TiO_2/Al_2O_3 ratio in comparison to the remaining lower section of the profile.

The gleisation is a molar ratio of Fe^{2+}/Fe^{3+} and is a commonly used elemental ratio. In this study, Fe^{2+}/Fe^{3+}
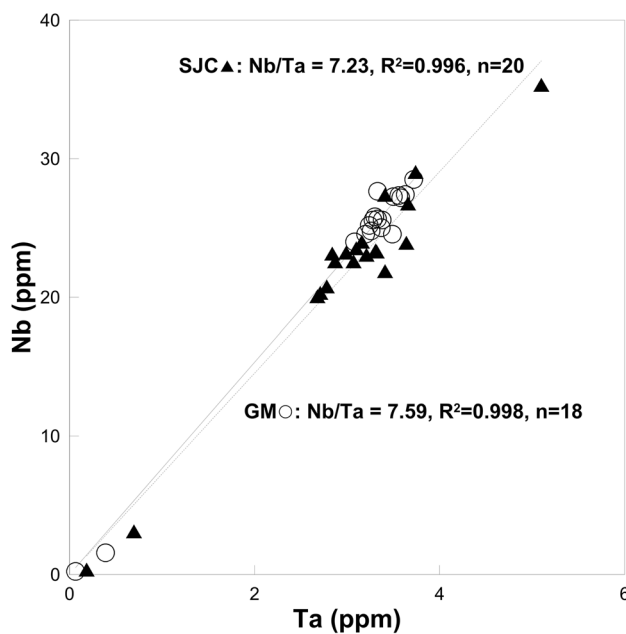
Fig. 7 The Nb vs. Ta (ppm) relationship for soil samples of San-jiacum (SJC) and Gumu (GM) profiles in Yunnan-Guizhou Plateau, Southwestern China

was calculated based on the FeO (mol.%)/[$2 \times$ Fe$_2$O$_3{}^T$ (mol.%) $-$ FeO (mol.%)]. This elemental ratio displayed similar trend at both profiles as shown in Fig. 3b. In addition, Fe/Na ratio can be used to determine soil maturity, based on the contrasting behaviour of Fe (enrichment) and Na (depletion) during pedogenesis. The Fe/Na ratio was constant in the red soil layers for both profiles as shown in Fig. 3c, except for a significant increase at the SJC9 ferricrete layer which was mainly due to enrichment in Fe oxides. See subsequent section for detailed discussion on this ratio.

The Ba/Sr ratio is an index used to determine leaching behaviour during weathering with values reflecting leaching activities, i.e. the higher the values, the more leaching activities occur. The results in Fig. 3f showed that, both profiles exhibited low Ba/Sr values in the bedrock and rock powder, but high and constant values (> 2) from the weathering front towards the top soils.

The U/Th ratio is a useful provenance indicator in paleosols that can determine whether material source have any foreign or external influence. Figure 3e showed relatively slight variation of U/Th ratio from weathering front to upper red soils for both soil profiles.

The CIA index often used in paleosols to characterised the weathering intensity within soil profile. According to Tables 1, 3, bedrock samples (GM1 and SJC1) had CIA values of 26 (weak chemical weathering) and 61 (moderate chemical weathering), respectively. Rock powder of both profiles had similarly high CIA values of 83 and 77,

respectively. However, of the two studied profiles, GM red soil layers exhibited a slightly higher CIA values (92–93) than the SJC red soil profile which had CIA values of 83–93. On comparing the bedrock CIA values with other samples, all samples of the soil profile had notably high CIA values, indicating intense chemical weathering for these materials.

Discussion

Mineralogy and geochemical characteristics of weathering profile

Chemical weathering can be influenced by rainfall, temperature, plant root, and tectonic movement; however, the parent rock lithology may also be a potential dominant driving force behind weathering (Chetelat et al. 2013). Therefore, it is important to evaluate the lithological influence on chemical weathering. This study examined mineralogy, geochemical and elemental ratios within red soil crust developed over dolomite and limestone bedrock of YG Plateau, to assess the behaviour of elements during the weathering and pedogenesis process.

Soil colour is usually a good indicator of the organic matter and iron content within the soil. As shown in Fig. 2, the soil colour in SJC profile varied from yellowish red (5YR 4/6) to light red (2.5YR 6/8); similar colour was also displayed in GM profile. The colours of these two studied soil profiles are quite similar with those of *terra rossa* or lateritic soils under Mediterranean climate (Bellanca et al. 1996; Feng et al. 2012; Giorgis et al. 2014; Lucke 2016; Wei et al. 2013). These hues indicate the presence of hematite and goethite in the soils either at high temperature or low water activity during pedogenetic conditions (Cornell and Schwertmann 2003). The XRD results further confirmed the presence of hematite and goethite distributed within both profiles (Fig. 4). The soil types in this study are mostly equivalent to oxisols, ultisols and some alfisols according to the soil taxonomic classification of USA. The mineral differences between the SJC and GM profiles shown in Fig. 4 may be due to the bedrock lithology difference. The mineral assemblage in both profiles are very similar to those in *terra rossa* at the western Sicily, Italy (Bellanca et al. 1996) and are similar to those in red soils at the Pingba profile located at YG Plateau (Ji et al. 2004a). From the XRD results (Fig. 4), the clay minerals within the red soils of SJC and GM profiles are generally constant along the vertical depths, except for the layer around SJC ferricrete layer. Both the SJC and GM profiles have been developed under subtropical monsoonal climate with distinct wet and dry conditions. These conditions are closely similar under which *terra rossa* is formed and also similar where the accumulation of secondary carbonate minerals occurred in Mediterranian regions.
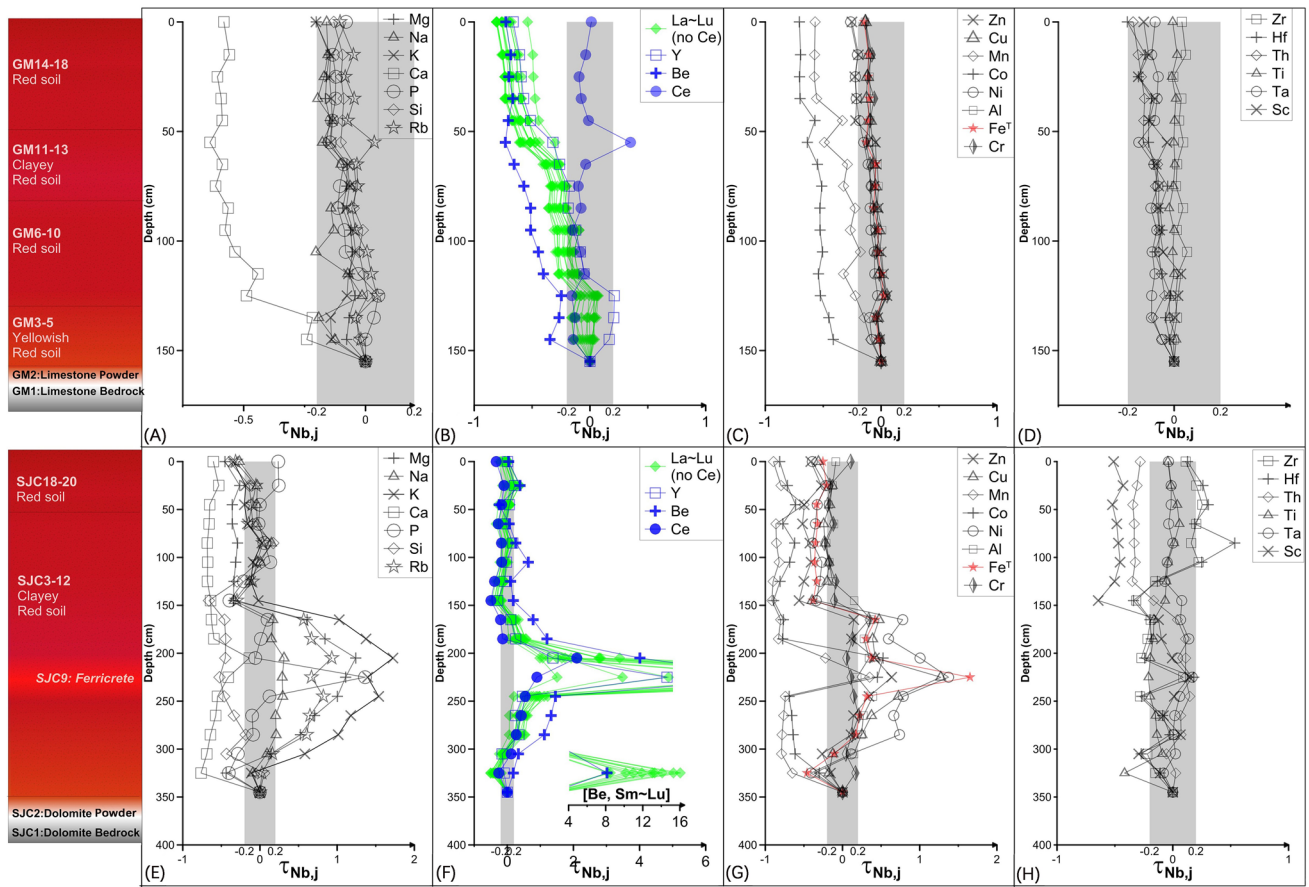
Fig. 8 Element transport efficiencies ($\tau_{Nb,j}$) vs. depth of GM (A–E) and SJC (F–J) profiles in Yunnan–Guizhou Plateau, Southwestern China
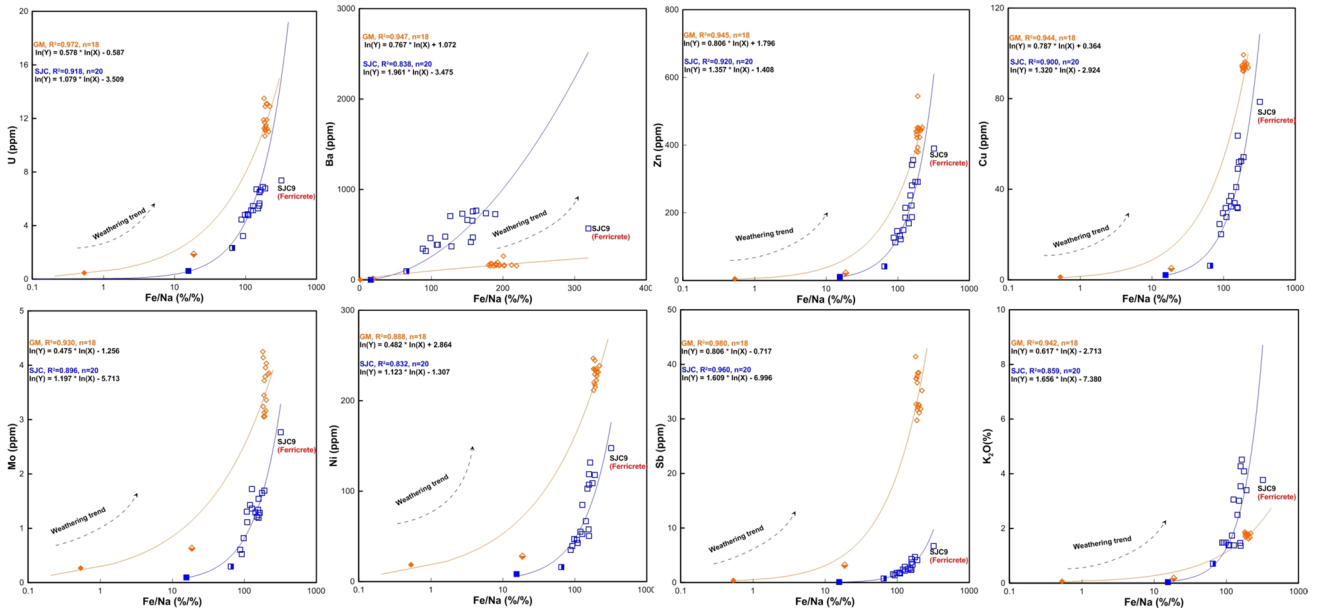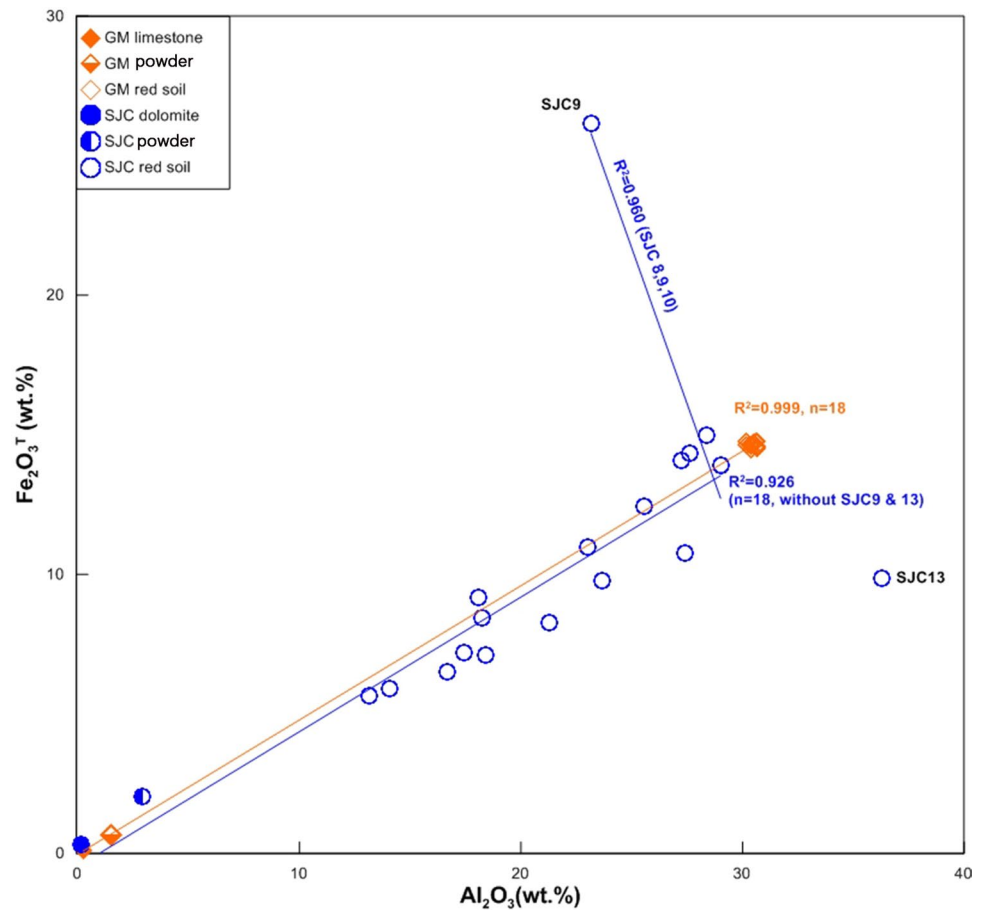

Fig. 9 Fe/Na ratio vs. elements (U, Ba, Zn, Cu, Mo, Ni, Sb, in ppm) and K_2O (%) in GM and SJC profiles in Yunnan–Guizhou Plateau, Southwestern China

Fig. 10 The $Fe_2O_3^T$ vs. Al_2O_3 of GM and SJC profiles in Yunnan–Guizhou Plateau, Southwestern China. The straight positive correlation line from bedrock to regolith indicates carbonate dissolution and accumulation weathering trend

The climatic condition in YG Plateau favoured the formation of gibbsite and diaspora, which are commonly formed in laterites, especially in upland regions of moist and subtropical zones. This is in accordance with the XRD analysis, which detected the presence of Al minerals (Fig. 4). In addition, around the ferricrete layer (SJC7–SJC11), aluminium minerals drastically decrease, indicating different geochemical behaviours which are consistent with the transport coefficiency τ of Al and Fe at SJC9 (Fig. 8g). This was due to the migration of Al as a result of chemical dissolution (Young and Nesbitt 1998).

During the chemical weathering process, elements such as Al, Ti and Fe are less mobile than other elements (Braun et al. 1993; Ji et al. 2004a, b; Nesbitt et al. 1982). Therefore, major oxides such as Al_2O_3, Fe_2O_3, and TiO_2 can be used effectively to determine source of materials and degree of weathering. According to Ji et al. 2004a, b, Al_2O_3/Fe_2O_3 ratio is an effective indicator for tracing material sources over carbonate areas and, hence, can be used as an index to evaluate *in situ* weathering. The positive straight correlation line from bedrock to regolith indicates dissolution and accumulation trend for GM soil profiles, which indicates *in situ* weathering (Young and Nesbitt 1998) and that Al_2O_3 and

Fe_2O_3 share similar immobile geochemical behaviour. While the positive linear correlation from the bedrock indicate dissolution and accumulation trend, SJC-9 and 13 however may suggest external contribution or influence. The negative correlation line for sample from ferricrete layer SJC-9 and samples from other layers (SJC-8, -9, -10) shows good correlation ($R^2 = 0.96$). This interpreted as Al and Fe in SJC profile shared similar geochemical behaviour (immobile) and that although the soil profile had inheritance from bedrock, there was some amount of external influence (Fig. 10). The point SJC13 showed a slight increase of Fe^{2+}/Fe^{3+} (more reducing condition) and pH (Fig. 3a, b), respectively, which could increase the solubility of Fe in the reducing and acid solution. Similarly, the Ti/Al ratio indicated to be least mobile during chemical weathering; however, their geochemical behaviours are different. The solubility of Fe is controlled by redox condition, while pH value controls the solubility of Al and Ti. The relationship between Ti/Al and depth is shown in Fig. 3d. The slight curve of Ti/Al in the SJC red soil layers (Ti/Al = 0.02 ~ 0.07) corresponds to that of pH variation, where the increase of pH leads to increase of insoluble of Al. However, constant Ti/Al in the red soil of GM is related to the consistent decrease of pH from alkaline to closely

neutral values where Al and Ti are insoluble. Therefore, the lower Ti/Al ratio in GM is mainly attributed to the enrichment of Al^{3+} minerals by intense weathering. Based on the mineralogy and geochemical evidence, these clay minerals were more likely to be formed from either *in situ* weathering products or metasomatic process rather than detrital process (external sources). Other evidence such as isotopic in future studies could possibly confirm the origin of the red soil in Yunnan–Guizhou Plateau, southwestern China.

Mobilisation and distribution of elements during pedogenesis and weathering

Based on the element transport efficiencies on weathering front for high field strength elements (HFSE) such as Nb, Ta, Zr, Hf, Th, and Sc otherwise called immobile elements, the elements were stable in both profiles, except for Th and Sc in SJC profile. This was illustrated by the transport efficiency $\tau_{j,w}$ values being close to zero, which may due to the weak influences by metamorphism, dissolvent, or weathering, except for peak values at the weathering front of crust (Zhang et al. 2014). The dramatic depletion of Th and Sc in SJC profile, whereby the other immobile elements (Zr, Hf, Ti, and Ta) remain relatively constant may indicate polygenic provenance. The relative stability of all the HFSE in GM profile was interpreted as characteristics of in situ weathering.

Alkali and alkaline earth element Rubidium has similar chemical characteristics as Potassium which may function similarly in minerals (Bauer and Velde 2014), and so soils of similar age in granitic materials displayed linear correlation in Rb vs. K plot (White et al. 2008). In SJC and GM profiles, it appears that K and Rb varied together according to Fig. 8a, e, which is an indication of possible similar pedogenesis periods of the soils in the two profiles, respectively.

The transitional metals (Co, Ni, Cu, Zn, Cr) are generally associated with Fe and Mn in high-temperature minerals which can be suitable candidates for substitution in iron oxide structures in the trivalent state. The distribution of Fe and Mn is redox sensitive; thus, transitional elements associated with Fe and Mn oxides/hydroxides will be redistributed into different mineralogical structures as iron or manganese changes oxidation state (Bauer and Velde 2014). The monsoonal climate resulting in strong spatial dynamics of soil water processes thereby controlled redox environment. In SJC and GM profiles, Mn and Co displayed close relationship during pedogenesis (Fig. 8c, g), respectively; while, Cu, Ni, Zn, Cr displayed close relationship with Fe and Al. It is reported that in bauxites, Co is closely related to Fe content than Mn; whereas, in layers with high concentration of Fe such as the ferricrete layer, Co appears to be more related to the Mn than to Fe (Bauer and Velde 2014).

The enrichment of rare earth elements is fairly common in weathering crust; whereas in most cases, well-developed crust indicates a parabolic distribution of total REEs in vertical soil profile, i.e., the enrichment occurs at the bottom of fully weathered crust. However, the patterns of REEs concentration during chemical weathering differ according to bedrock types and weathering conditions. Usually, the fluctuation of pH values is the primary reason for REE enrichment within weathering crust (Gouveia et al. 1993). During the downward infiltration of underground water, chemical weathering of minerals (included REE minerals) absorbed large amount of H^+, resulting in an increase of pH values in the GM profile. At the semi-weathering layer, the adsorption of water is less at the bottom-weathered layer resulting in the parabolic distribution of REEs. The close relationship between REEs and Y was widely reported on due to their geochemical similarities (Elderfield and Greaves 1981; Feng 2010; Glasby et al. 1987; Pattan et al. 2005). The SJC and GM profiles showed similar trend according to Fig. 8b, f. Beryllium (Be) isotope has been widely used as a tracer in geochemical events (Edmunds 2011). Beryllium was slightly affected by weathering processes (Grigor'yev 1986). Based on the SJC and GM profiles as shown in Fig. 8b, f, Beryllium displayed close relationship with REEs and Y.

The negative and positive Ce abnormality is geochemically unique under low temperature and pressure conditions within the earth's crust. In carbonate weathering crust, Ce usually exhibited negative abnormality in REE spider diagrams (Ji et al. 2004b). However, for this study, there was exception as some layers exhibited positive Ce abnormalities (Fig. 6b, d). Most carbonate rocks display a negative Ce anomaly due to ionic radii and coordination numbers (Laveuf and Cornu 2009). Hence, the negative Ce anomaly especially at the points close to the bedrock is inherited from the dolomite bedrock. During chemical weathering, Ce^{3+} is readily oxidised to Ce^{4+} and precipitate as CeO_2 (Braun et al. 1990; Yusoff et al. 2013). Therefore, the increase in Ce results from oxidising conditions. Furthermore, Bradbury and Baeyens (2002), and Tertre et al. (2006) reported that the metal exchange reactions are pH and temperature independent in acidic and closely neutral range under 80 °C, whereas surface complexion reactions are endothermic and predominant under neutral and alkaline conditions. The transport efficiency of Ce based on weathering front was relatively stable in GM profile, and similarly stable for SJC profile, except for enrichment around ferricrete layer, although temperature and pH varied during the pedogenesis. Therefore, the enrichment of Ce around the ferricrete layer (Fig. 8f) could be due to the presence of secondary cerianite of weathering origin (Feng 2010).

Elemental ratios during chemical weathering

Generally, most studies used variation of element ratios or transport coefficient to examine the behaviour of elements along the vertical depth on lateritic soils or *terra rossa* (Calagari et al. 2015; Giorgis et al. 2014; Wei et al. 2014; Zhang et al. 2014, 2015).

The Ba/Sr ratio is an index used to represent leaching behaviour during weathering (Retallack 2010; Sheldon 2006; Sheldon and Tabor 2009) higher values indicate more leaching activities. Both Ba and Sr are alkaline earth elements and have similar atomic radii and chemical affinities. However, Sr is significantly more soluble than Ba (Vinogradov 1959); therefore, Sr will be leached more readily under most conditions. Retallack (1997) suggested that Ba/Sr ratio values in excess of 2 indicate acidic/leached conditions. Both profiles exhibited low Ba/Sr values in the bedrock and rock powder, but high and constant values (> 2) from the weathering front towards the top soils (Fig. 3f). This is a clear indication that both profiles experienced some amount of leaching activities, which is a consequence of chemical weathering.

The U/Th ratio is probably the most useful provenance indicator in paleosols with a short moderate formation time (Sheldon and Tabor 2009). The relatively small variation of U/Th ratio from weathering front to upper red soils for GM profile may be interpreted as in situ weathering, while the slightly higher variation for SJC profile may be considered as influence of external or foreign materials (Fig. 3e).

Lithium is present in many geological environments in small quantities and is closely related to aluminium in soil, hence high probability to be present in clay minerals (Bauer and Velde 2014). Mineral such as sodium birnessite could fixed Li in their lattice. This retention of Li can be associated within manganese minerals or aluminous clay minerals (Bauer and Velde 2014). In our study, both SJC and GM profiles indicated a close dependent relationship between Li and Al_2O_3 ($R^2 > 0.95$), which may be due to the enrichment of Li and Al in clay minerals during pedogenesis (Fig. 11).

Fe/Na ratio in quantification of chemical weathering in carbonate crust

CIA index is commonly proposed as an indicator of weathering intensity for soil profiles. However, for intense weathering soils, the CIA values do not seem to provide good indicative information on weathering. In light of this, a more useful potential indicator, i.e. Fe/Na ratio is applied in this study. The Fe/Na ratio indicates high correlation with some element concentrations (Fig. 9), especially for the elements U and Ba which indicate a "U"-shaped power function relationship (Garrett and Lalor 2005). It is noticeable that the K

vs. Fe/Na of SJC profile showed weathering trend above and below the ferricrete layer, where the black line represents the soils below ferricrete layer and red lines represent the upper. The increase in K_2O below the ferricrete layer is related to the enrichment of K minerals such as feldspar and kaolinite, while the decrease in K_2O result from leaching of K bearing minerals. Nevertheless, there seems to be no direct relationship between fluctuation of red soil and Fe/Na ratio. The lanthanide series such as La, Eu and Yb showed decreasing trend with depth. In addition, the element Be showed similar trend with lanthanide elements, which coincides with the transport efficiency trend (Fig. 8b, f).

The Fe/Na ratio was proposed to be related with trace elements in soils with particle size of less than 150 micron in diameter (Garrett and Lalor 2005). The elements U, As, Ba, Lu vs. Fe/Na ratio exhibited "U"-shape-type patterns in binary plots (Fig. 9). The Fe/Na ratio was explored to distinguish maturity among different soils of oxisols, mollisols and inceptisols (Garrett and Lalor, 2005). The carbonate weathering crust is ideal for studying weathering and pedogenesis. Our study applied Fe/Na ratio to investigate the red soil over carbonate, and the results revealed that it could be used to determine source. Strong correlations ($R^2 \approx 0.90$) of power function were common in the studied profiles (Fig. 9). It is expected that with the least addition of different sources into the profile, the higher the coefficiencies of the power function between Fe/Na ratio and other elements.

Conclusions

The two studied soil profiles over carbonate rocks (GM-limestone and SJC-dolomite) at Yunnan–Guizhou Plateau, southwestern China has the typical characteristics of red soils with high maximum SiO_2 (35.45 and 73.6%), Fe_2O_3 (14.75 and 26.2%), and Al_2O_3 (30.68 and 36.3%) contents, respectively. The characteristic of being neutral or slightly alkaline in nature may have influenced elemental mobilisation and leaching during weathering and pedogenesis. Both profiles have experienced intense chemical weathering in the soil and saprolite with high average CIA values of 87.7 and 92.5. The profiles also experienced a constant Ba/Sr ratio > 2 from weathering front upwards to the soil surface, which indicate leaching activities. The XRD analysis revealed similarities in secondary minerals distribution (kaolinite, gibbsite. anatase) in the red soils, with exception at the ferricrete layer. In addition, the results further confirmed the presence of hematite and goethite distributed within both profiles. The mineral assemblages in both profiles are found to be similar to those in *terra rossa* at the western Sicily, Italy and those red soils at the Pingba profile located at YG Plateau. The UCC normalisation of major and trace elements displayed significant enrichment in all the elements except Sr in both
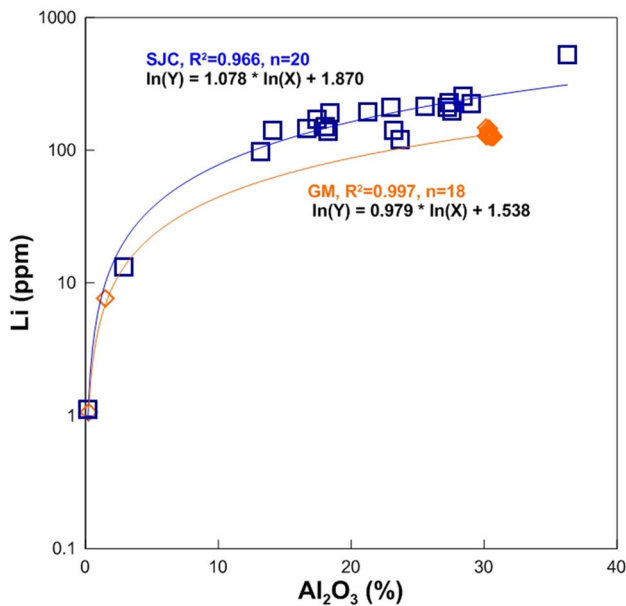
Fig. 11 Li (ppm) vs. Al$_2$O$_3$ (%) of GM and SJC profiles in Yunnan–Guizhou Plateau, Southwestern China

profiles. The REE distribution pattern revealed light-REE enrichment for both profiles, also each profile possesses one distinct layer with super concentration of REEs (i.e., at the weathering front for GM profile and at the ferricrete layer for SJC profile) other than the bedrock powder. Based on the geochemical evidence to include major, trace, REE and elemental ratios, the GM profile was derived from in situ weathering, while SJC profile although had influence from underlying bedrock also had contribution or influence from external source.

The mass balance calculation along the vertical profile using the weathering front soil as reference indicated that K and Rb are closely related during evolution of profile. Furthermore, all the lanthanide elements except Ce shared similar transport trends with Y and Be; in addition, Be exhibited significant enrichment at ferricrete layer of the dolomite profile. The transitional elements Co and Mn behave similarly in comparison to other transition elements such as Zn, Cu, Ni and Cr. The HFSE are stable during soil profile evolution, except for Th and Sc, which experienced depletion in upper soil layer of SJC profile. Both profiles experienced similar elemental behaviour during chemical weathering with the accumulation of major elements, the leaching of alkaline earth elements and the fluctuation of trace elements including REEs which were primarily controlled by redox reaction, pH, water availability, ionic radii and the stability of secondary oxides/hydroxides. The small variations in geochemical characteristics and behaviour of elements during weathering and pedogenesis were due to lithology and physiochemical properties. Finally, Fe/Na ratio was proposed and analysed

for this carbonate weathering crust, whereby Fe/Na vs. U can be used as a profile-dependent weathering index over Yunnan–Guizhou Plateau.

References

Anderson SP, Dietrich WE, Brimhall GH (2002) Weathering profiles, mass-balance analysis, and rates of solute loss: linkages between weathering and erosion in a small, steep catchment. Geol Soc Am Bull 114:1143–1158

Babechuk MG, Widdowson M, Kamber BS (2014) Quantifying chemical weathering intensity and trace element release from two contrasting basalt profiles, Deccan Traps. India Chem Geol 363:56–75

Babechuk MG, Widdowson M, Murphy M, Kamber BS (2015) A combined Y/Ho, high field strength element (HFSE) and Nd isotope perspective on basalt weathering, Deccan Traps, India. Chem Geol 396:25–41

Banerjee A, Merino E (2011) Terra Rossa genesis by replacement of limestone by kaolinite. III. Dynamic quantitative model. J Geol 119:259–274

Bates RL, Jackson JA (1987) Glossary of geology. American Geological Institute, Falls Church

Bauer A, Velde BD (2014) Geochemistry at the Earth's Surface: movement of chemical elements. Springer, Heidelberg New York Dordrecht London

Bautista F, Palacio-Aponte G, Quintana P, Zinck JA (2011) Spatial distribution and development of soils in tropical karst areas from the Peninsula of Yucatan, Mexico. Geomorphology 135:308–321

Bellanca A, Hauser S, Neri R, Palumbo B (1996) Mineralogy and geochemistry of Terra Rossa soils, western Sicily: Insights into heavy metal fractionation and mobility. Sci Total Environ 193:57–67

Boeglin JL, Probst JL (1998) Physical and chemical weathering rates and CO$_2$ consumption in a tropical lateritic environment: the upper Niger basin. Chem Geol 148:137–156

Bradbury MH, Baeyens B (2002) Sorption of Eu on Na- and Ca-montmorillonites: experimental investigations and modelling with cation exchange and surface complexation. Geochim Cosmochim Acta 66:2325–2334

Brantley SL, Lebedeva M (2011) Learning to read the chemistry of regolith to understand the Critical Zone. Ann Rev Earth Plan Sci 39:387–416

Braun JJ, Pagel M, Muller JP, Bilong P, Michard A, Cuillet B (1990) Cerium anomalies in lateritic profiles. Geochim Cosmochim Acta 54:781–795

Braun JJ, Marechal JC, Riotte J, Boeglin JL, Bedimo JPB, Ngoupayou JRN, Nyeck B, Robain H, Sekhar M, Audry S et al (2012) Elemental weathering fluxes and saprolite production rate in a Central African lateritic terrain (Nsimi, South Cameroon). Geochim Cosmochim Acta 99:243–270

Brimhall GH, Dietrich WE (1987) Constitutive mass balance relations between chemical composition, volume, density, porosity, and strain in metasomatic hydrochemical systems: Results on weathering and pedogenesis. Geochim Cosmochim Acta 51:567–587

Buggle B, Glaser B, Hambach U, Gerasimenko N, Marković S (2011) An evaluation of geochemical weathering indices in loess–paleosol studies. Quatern Int 240:12–21

Calagari A, Kangarani F, Abedini A (2015) Geochemical characteristics of a laterite: the Jurassic Zan Deposit. Iran Acta Geodyn Geomater 12:67–77

Chetelat B, Liu C-Q, Wang Q, Zhang G (2013) Assessing the influence of lithology on weathering indices of Changjiang river sediments. Chem Geol 359:108–115

Cornell RM, Schwertmann U (2003) The iron oxides: structure, properties, reactions, occurrences and uses. John Wiley & Sons, 664

Dobrovolsky EV (1987) Proceedings of an International Seminar on Laterite Physico-chemical mechanisms of weathering processes and corresponding models of dynamics of mineral zonality evolution. Chem Geol 60:89–94

Duan X, Tao Y (2012) The climate change of Yunnan over the last 50 years. J Tropical Meterol 243–250

Duan JZ, Xue SR, Qian XG (2001) The Cenozoic geological tectonic framework and evolution in the Three River Area of West Yunnan. Yunnan Geol 243–252

Durn G, Ottner F, Slovenec D (1999) Mineralogical and geochemical indicators of the polygenetic nature of terra rossa in Istria, Croatia. Geoderma 91:125–150

Durn G, Aljinović D, Crnjaković M, Lugović B (2007) Heavy and light mineral fractions indicate polygenesis of extensive terra rossa soils in Istria, Croatia. In: Maria AM, David TW, eds. Developments in Sedimentology, (Elsevier), pp. 701–737

Durn G, Hrenovic J, Sekovanic L (2013) Terra rossa as the substrate for biological phosphate removal from wastewater. Clay Min 48:725–738

Durn G, Coric R, Tadej N, Barudzija U, Rubinic V, Husnjak S (2014) Bulk and clay mineral composition indicate origin of terra rossa soils in Western Herzegovina. Geol Croat 67:171–183

Edmunds WM (2011) Beryllium: Environmental Geochemistry and Health Effects A2—Nriagu JO In Encyclopedia of Environmental Health (Burlington: Elsevier), pp. 293–301

Elderfield H, Greaves MJ (1981) Negative cerium anomalies in the rare earth element patterns of oceanic ferromanganese nodules. Earth Planet Sci Lett 55:163–170

Fedo CM, Nesbitt HW, Young GM (1995) Unraveling the effects of potassium metasomatism in sedimentary rocks and paleosols, with implications for paleoweathering conditions and provenance. Geology 23:921

Feng JL, Zhu LP (2009) Origin of terra rossa on Amdo North Mountain on the Tibetan plateau, China: evidence from quartz. Soil Sci Plant Nutr 55:407–420

Feng JL (2010) Behaviour of rare earth elements and yttrium in ferromanganese concretions, gibbsite spots, and the surrounding terra rossa over dolomite during chemical weathering. Chem Geol 271:112–132

Feng JL, Lin YC, Gao SP, Zhang JF (2012) Enrichment of trace elements in ferromanganese concretions from terra rossa and their potential desorption. Geochem J 46:151–161

Garrett RG, Lalor GC (2005) The Fe/Na ratio, a framework for modelling trace element distributions in Jamaican soils. Geochem Explor Env A 5:147–157

Giorgis I, Bonetto S, Giustetto R, Lawane A, Pantet A, Rossetti P, Thomassin JH, Vinai R (2014) The lateritic profile of Balkouin, Burkina Faso: geochemistry, mineralogy and genesis. J Afr Earth Sci 90:31–48

Glasby GP, Gwozdz R, Kunzendorf H, Friedrich G, Thijssen T (1987) The distribution of rare earth and minor elements in manganese nodules and sediments from the equatorial and S.W. Pacific Lithos 20:97–113

Gong QJ, Zhang GX, Zhang J, Jiang BA, Ma N (2010) Behaviour of REE fractionation during weathering of dolomite regolith profile in Southwest China. Acta Geol Sin-Engl 84:1439–1447

Gong QJ, Deng J, Yang LQ, Zhang J, Wang QF, Zhang GX (2011) Behaviour of major and trace elements during weathering of sericite-quartz schist. J Asian Earth Sci 42:1–13

Gouveia MA, Prudêncio MI, Figueiredo MO, Pereira LCJ, Waerenborgh JC, Morgado I, Pena T, Lopes A (1993) Third international symposium on the geochemistry of the earth surface behaviour of REE and other trace and major elements during weathering of granitic rocks, Évora. Portugal Chem Geol 107:293–296

Grigor'yev NA (1986) Distribution of Beryllium at the surface of the earth. Int Geol Rev 28:327–371

Harnois L (1988) The CIW index: a new chemical index of weathering. Sediment Geol 55:319–322

Huang ZG, Zhang WQ, Chen JH (1998) The red earth periods in China. Tropical Geogr 18:34–41

Ji HB, Wang SJ, Ouyang ZY, Zhang S, Sun CX, Liu XM, Zhou DQ (2004a) Geochemistry of red residua underlying dolomites in karst terrains of Yunnan-Guizhou Plateau I. The formation of the Pingba profile. Chem Geol 203:1–27

Ji HB, Wang SJ, Ouyang ZY, Zhang S, Sun CX, Liu XM, Zhou DQ (2004b) Geochemistry of red residua underlying dolomites in karst terrains of Yunnan-Guizhou Plateau II. The mobility of rare earth elements during weathering. Chem Geol 203:29–50

Kahmann JA, Seaman J, Driese SG (2008) Evaluating trace elements as paleoclimate indicators: multivariate statistical analysis of late Mississippian Pennington Formation paleosols, Kentucky, USA. J Geol 116:254–268

Kronberg BI, Nesbitt HW (1981) Quantification of weathering, soil geochemistry and soil fertility. J Soil Sci 32:453–459

Kurtz AC, Derry LA, Chadwick OA, Alfano MJ (2000) Refractory element mobility in volcanic soils. Geology 28:683–686

Laveuf C, Cornu S (2009) A review on the potentiality of rare earth elements to trace pedogenetic processes. Geoderma 154:1–12

Li JY, Zhu LJ (2004) On modern weathering crust and palaeo-weathering crust of carbonate rock. Carsol Sinica. 57–63

Li JY, Zhu LJ, Wang CF, Fan YZ, Chen J (1996) Weathering crust of carbonate rocks and process of karst soil formation. Guizhou Geol 13:139–145

Li J, Zhu L, Liang F (2000) Characteristics of structure and mineralogy of interface laterite in weathering crust of carbonate rocks. Carsol Sinica 19:11–17

Li JY, Zhu LJ, Liang F, Chen J (2002) Study with scanning electron microscope on micro-texture of the residual red clay from carbonate rocks. Carsol Sinica 21:233–237

Lu YR (1986) Models of karst geomorphological evolutions in China. Geogr Res 5:25–35

Lucke B (2016) Correlation of soil color, redness ratings, and weathering indices of Terrae Calcis along a precipitaion gradient in northern Jordan. Erlanger Geographische Arbeiten Band, Chapter 5- Correlation of color and weathering indices of Terrae Calcis 42: 53–68

Lucke B, Kemnitz H, Baumler R (2012) Evidence for isovolumetric replacement in some Terra Rossa profiles of northern Jordan. B Soc Geol Mex 64:21–35

Lucke B, Kemnitz H, Baumler R, Schmidt M (2014) Red Mediterranean Soils in Jordan: new insights in their origin, genesis, and role as environmental archives. CATENA 112:4–24

Merino E, Banerjee A (2008) Terra rossa genesis, implications for karst, and eolian dust: a geodynamic thread. J Geol 116:62–75

Moresi M, Mongelli G (1988) The relation between the terra rossa and the carbonate-free residue of the underlying limestones and dolostones in Apulia. Italy Clay Miner 23:439–446

Muhs DR, Budahn JR (2009) Geochemical evidence for African dust and volcanic ash inputs to terra rossa soils on carbonate reef terraces, northern Jamaica, West Indies. Quatern Int 196:13–35

Nesbitt HW (1979) Mobility and fractionation of Rare-Earth elements during weathering of a granodiorite. Nature 279:206–210

Nesbitt HW, Markovics G, Price RC (1980) Chemical processes affecting alkalis and alkaline earths during continental weathering. Geochimica et Comochimica Acta 44:1659–1666

Nesbitt HW, Young GM (1982) Early proterozoic climates and plate motions inferred from major element chemistry of lutites. Nature 299:715–717

Palme H, Jones A (2005) Solar system abundances of the element, in Meteorite, Comets, and Planets, Treatise on Geochemistry. Amsterdam, Elisevier 1 (ed. A.M. Davis), 41–62

Pattan JN, Pearce NJG, Mislankar PG (2005) Constraints in using Cerium-anomaly of bulk sediments as an indicator of paleo bottom water redox environment: a case study from the Central Indian Ocean Basin. Chem Geol 221:260–278

Retallack GJ (1997) A colour guide to paleosols. John Wiley and Sons, Chichester (UK), p 175

Retallack GJ (2010) Lateritization and Bauxitization Events. Econ Geol 105:655–667

Sheldon ND (2006) Abrupt chemical weathering increase across the Permian-Triassic boundary. Palaeogeogr Palaeocl 231:315–321

Sheldon ND, Tabor NJ (2009) Quantitative paleoenvironmental and paleoclimatic reconstruction using paleosols. Earth-Sci Rev 95:1–52

Smykatz-Kloss B (2003) The loess occurrence of the Pleiser Hügelland near Bonn and Neustadt/Wied as well as Picardy: mineralogical geochemical and geomorphological characterization, weathering influence and origin of the loess. (University of Bonn)

Šušteršič F, Rejšek K, Mišič M, Eichler F (2009) The role of loamy sediment (terra rossa) in the context of steady state karst surface lowering. Geomorphology 106:35–45

Taylor SR, McLennan SM (1985) The continental crust: its composition and evolution. Blackwell Scientific Publication, Oxford, p 311

Tertre E, Berger G, Simoni E, Castet S, Giffaut E, Loubet M, Catalette H (2006) Europium retention onto clay minerals from 25 to 150°C: experimental measurements, spectroscopic features and sorption modelling. Geochim Cosmochim Acta 70:4563–4578

Vinogradov AP (1959) The geochemistry of rare and dispersed chemical elements in soils, 2nd ed., rev. and enl edn (Consultants Bureau Chapman & Hall)

Walter AV, Nahon D, Flicoteaux R, Girard JP, Melfi A (1995) Behaviour of major and trace elements and fractionation of REE under tropical weathering of a typical apatite-rich carbonatite from Brazil. Earth Planet Sci Lett 136:591–602

Wang SJ, Feng ZG (2004) Heterogeneity of parent rocks and its constraints on geochemical criteria in weathering crusts of carbonate rocks. Acta Geol Sin-Engl 78:1143–1153

Wang SJ, Ji HB, Ouyang ZY, Zhou DQ, Zheng YP, Li TY (1999) Preliminary Study on weathering and pedogenesis of carbonate rock. Science in China (Series D:Earth Sciences), 572–581

Wang Y, Peng SH, Yang SL (2012) The anomaly features of As and Cd in the karst area in Yunnan province. Carsologica Sinica 31:377–381

Wei X, Ji HB, Li DJ, Zhang FL, Wang SJ (2013) Material source analysis and element geochemical research about two types of representative bauxite deposits and terra rossa in western Guangxi, southern China. J Geochem Explor 133:68–87

Wei X, Ji H, Wang S, Chu H, Song C (2014) The formation of representative lateritic weathering covers in south-central Guangxi (southern China). CATENA 118:55–72

White AF, Schulz MS, Vivit DV, Blum AE, Stonestrom DA, Anderson SP (2008) Chemical weathering of a marine terrace chronosequence, Santa Cruz, California I: interpreting rates and controls based on soil concentration-depth profiles. Geochim Cosmochim Acta 72:36–68

Widdowson M, Cox KG (1996) Uplift and erosional history of the Deccan Traps, India: evidence from laterites and drainage patterns of the Western Ghats and Konkan Coast. Earth Planet Sci Lett 137:57–69

Xi CF (1991) On the red weathering crusts of Southern China. Quaternary Sci 11:1–8

Yang SY, Li CX, Yang DY, Li XS (2004) Chemical weathering of the loess deposits in the lower Changjiang Valley, China, and paleoclimatic implications. Quatern Int 117:27–34

Young GM, Nesbitt HW (1998) Processes controlling the distribution of Ti and Al in weathering profiles, siliciclastic sediments and sedimentary rocks. J Sediment Res 68:448–455

Yuan D (1992) Karst in southwest china and its comparison with karst in north china (in Chinese). Quaternary Sci 4:352–361

Yusoff ZM, Ngwenya BT, Parsons I (2013) Mobility and fractionation of REEs during deep weathering of geochemically contrasting granites in a tropical setting, Malaysia. Chem Geol 349–350:71–86

Zhang FL, Ji HB, Wei X, Li DG (2014) Geochemical characteristics of trace elements in a dolomite weathering profile in central Guizhou province. Earth Environ 42:611–619

Zhang L, Ji HB, Gao J, Li R, Li JJ (2015) Geochemical characteristics of major, trace and rare earth elements in typical carbonate weathered profiles of Guizhou Plateau. Geochimica 44:323–336

Zhao Q (1996) Red soils of hilly region in China: ecological environment and strategies for integrated development. In: Sehgal J, Blume WE, Gajbhiye KS, (eds.) Red and lateritic Soils, pp. 53–58

Zhu XM (1993) Red clay and red residuum in South China. Quaternary Sci 13:75–84

Zhu LJ, Li JY (2002) Metasomatic mechanism of weathering-pedogenesis of carbonate rocks: I. Mineralogical and microtextual evidence. J Guizhou Univ Technol (Natural Science Edition) 31:44–47

Zhu LJ, Fu PQ, Li JY (1996) Clay minerals in the laterite developed from carbonate rocks in Guizhou province and their forming mechanism. Acta Mineral Sinica 16:290–297